The Miocene Brahma porphyry Cu-Mo prospect in Central Chilean Andes (35°45′S): Geology, geochronology (U-Pb, Re-Os) and geochemistry

Valentina Díaz[a,b], Marcia Muñoz-Gómez[b,c,*], Katja Deckart[a,b], Brian Townley[a,b], Ryan Mathur[d], Osvaldo Martínez[a]

[a] Departamento de Geología, Universidad de Chile, Casilla 13518, Correo 21, Santiago, Chile
[b] Advanced Mining Technology Center (AMTC), Facultad de Ciencias Físicas y Matemáticas, Universidad de Chile, Av. Tupper 2007, Santiago, Chile
[c] Escuela de Ciencias de la Tierra, Facultad de Ingeniería, Universidad Andres Bello, Campus República, Salvador Sanfuentes 2357, Santiago, Chile
[d] Department of Geology, Juniata College, Huntingdon, PA 16652, USA

ARTICLE INFO

ABSTRACT

The Brahma prospect is a Neogene porphyry copper deposit located in the Chilean Andes at ~ 35°45′S, beyond the southerly extension of the previously defined Mio-Pliocene metallogenic belt of Central Chile. We present the results of a comprehensive study of this prospect based on drill hole logging, petrography, geochemistry, and geochronology, with the aim of constraining its paragenesis and formation within the metallogenic background of the region. The prospect is hosted by dioritic and granodioritic equigranular units mineralized by fluids from at least two hydrothermal pulses in turn related to the emplacement of porphyritic intrusives and hydrothermal breccias. Existing exploration drill holes only intercepted the phyllic and argillic zone of the system, consistent with the paucity of potassic alteration and the dominance of pyrite, sphalerite, chalcopyrite and molybdenite mineralization. Zircon U-Pb determinations of the main igneous units present yielded ages of ~ 17 Ma, 14 Ma, and 9 Ma. Mineralization ages of ~ 14 Ma, 12 Ma, and 10 Ma were obtained by Re-Os determinations on molybdenite from samples of different paragenetic stages. These data indicate that (i) the prospect is composed of at least three main magmatic events, (ii) early mineralization is associated with the ~ 14 Ma magmatic pulse, and (iii) economic mineralization occurred at ~ 10 Ma and lasted until at least 9 Ma, as indicated by the presence of a younger mineralized porphyritic unit of this age. The obtained ages are comparable to those reported for the Los Pelambres deposit, a Cu-Mo porphyry located at 31°43′S and belonging to the Mio-Pliocene Metallogenic Belt of Central Chile. For the main intrusive units recognized in the Brahma prospect, whole rock geochemical analyses reveal arc affinities, juvenile signatures, and the involvement of amphibole in the fractionating assemblages. In a whole, our results support the existence of a complex deep magmatic reservoir that fed the magmatic-hydrothermal system for a long period, of at least 4 to 5 m.y., a common characteristic in other Miocene-Pliocene deposits in Chile and also in porphyry Cu deposits worldwide. In addition, our results highlight an interesting exploratory potential for the Brahma prospect, a long-lived Cu-Mo porphyry deposit of early Miocene age which southerly expands until ~ 36°S the Mio-Pliocene Metallogenic Belt of Central Chile.

1. Introduction

The Chilean Andes margin corresponds to one of the most richly endowed copper provinces in the world and most of its resources are from Porphyry Cu (-Mo, -Au) deposits. These include the largest ones discovered up to date in the world, as Chuquicamata (22°16′S), Río Blanco-Los Bronces (33°12′S), and El Teniente (34°05′S), along with numerous other comparatively smaller deposits currently under exploitation (Fig. 1a; e.g. Camus, 2003; Maksaev et al., 2007). Such

characteristic has historically made the Chilean margin particularly attractive for exploration oriented to the discovery of porphyry Cu deposits. Given the vigorous and long-standing development of such activities, currently there seems to be no exposed resources left, which has led to both: (i) a change in the exploration techniques towards a more penetrative and integral approach and (ii) the search for new target areas among those previously disregarded as highly fertile.

Porphyry Cu deposits correspond to large volumes of hydrothermally altered rocks centered on porphyry stocks associated to late
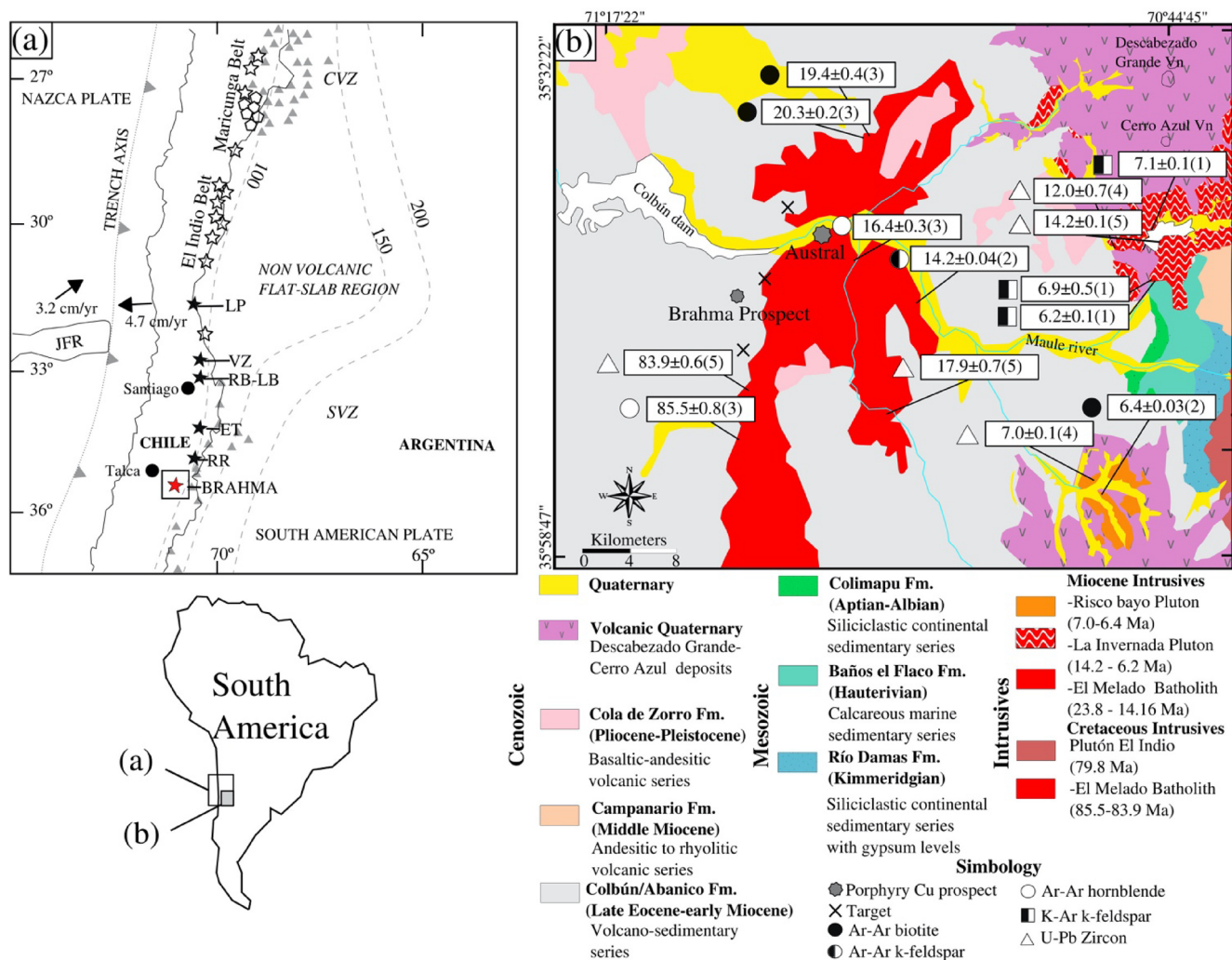
Fig. 1. (a) Main tectonic features of the Central Chilean margin modified from Charrier et al. (2007). The map shows the distribution of volcanoes (gray triangles) constituting the Central and Southern volcanic zones (CVZ and SVZ) and the depth contours of the Wadati-Benioff plane (Cahill and Isacks, 1992).The zone between 27°S to 33°S corresponds to the non-volcanic flat-slab region. The black stars show the location of the Neogene porphyry copper deposits in Central Chile, white stars indicate precious metal epithermal deposits and white pentagons indicate Au porphyries (Maksaev et al., 2007). JFR: Juan Fernández ridge, LP: Los Pelambres, VZ: Vizcachitas, RB-LB: Río Blanco-Los Bronces, ET: El Teniente, RR, Rosario de Rengo. (b) Regional scale geology of the western slope of the Andes Cordillera nearby the Colbún area (35°46′S). Simplified map from Sernageomin (2003) and Astaburuaga (2014). Geochronological data of the main intrusive units taken from (1) Drake (1976), (2) Nelson et al. (1999), (3) Spikings et al. (2008), (4) Astaburuaga (2014) and (5) Cabezas et al. (2018).

volcano-plutonic arc activity (e.g. Richards, 2003, 2005; Sillitoe, 2010). They are inferred to result from the favorable confluence of a series of specific geological factors and/or processes, which operating altogether, prompt their formation (e.g. Richards, 2003, 2005; Sillitoe, 2010). Throughout its evolution, regional scale formation of porphyry deposits has occurred repeatedly along the Chilean Andes margin, but during relatively short time spans and at specific moments during the lifetime of the coeval hosting magmatic arc (for reviews see Camus, 2003; Maksaev et al., 2007). As resulting from such specific episodes, porphyry deposits in the area have been classically grouped in metallogenic belts that distribute along strike of the Chilean margin (for reviews see Camus, 2003; Maksaev et al., 2007). The youngest of these corresponds to the Miocene-Pliocene metallogenic belt, which hosts highly endowed Cu-Mo porphyry deposits between ~ 32° and 34°S and Au-rich porphyry and epithermal deposits further north (Fig. 1a; e.g. Camus, 2003; Maksaev et al., 2007). The southern termination of this belt is marked by the El Teniente mega-deposit (34°05′S); however, the push to explore in previously underestimated areas has attracted interest in the extension of this metallogenic belt in the region further south. In such region, several prospects have been found (Fig. 1a), but

they remain under early exploration activities and their full metallogenic and economic potential remains to be determined. One of these prospects and the focus of the present study corresponds to the Miocene Brahma porphyry Cu-Mo prospect, located in the Andean main range in the Maule region at ~ 36°S (Fig. 1).

The Brahma prospect is located on the western slope of the Chilean Andes, at 35°46′S, in the southern shore of the Maule river, and 200 km south-southwest of the El Teniente Cu-Mo mega-deposit (Fig. 1a). In this contribution we present the results of a comprehensive study of this prospect based on drill hole logging, petrography, U-Pb and Re-Os age determinations, Lu-Hf isotopic compositions and whole-rock geochemical analyses. Our results indicate that this corresponds to a Miocene porphyry Cu-type mineralization event, whose economic potential is yet to be determined, therefore suggesting an important southerly extension of the Chilean Miocene belt.

2. Geological background

2.1. Tectonic setting and geology of the study area

The Chilean Andes runs along an active continental margin corresponding with the eastward subduction of the Nazca oceanic plate beneath the South American plate (Fig. 1a). Such a configuration has been continuous, but not steady, at least since the early Jurassic and is the first order control on the geological evolution of the upper continental plate (e.g. Charrier et al., 2007, 2015). The area where the Brahma prospect is located corresponds to the Southern Central Andes, which is distributed between ~ 33° to 46°S, immediately south of the so called flat-slab segment (~27°–33°S; Cahill and Isacks, 1992; Fig. 1a). The current tectonic configuration of the study region is characterized by a convergence rate of ~ 7 cm/yr with an obliquity of ~ 20° (Somoza and Ghidella, 2005) and a subduction dip angle of ~ 27° (Fig. 1a; Pardo et al., 2002). The active volcanic arc of this area runs along the highest summits of the Andean range, which marks the drainage divide and delineates the Chile-Argentina international border (Fig. 1a).

The geology of the western slope of the Andes Principal Cordillera is dominated by rock outcrops of Cenozoic and Mesozoic ages. These distribute in nearly NS-trending belts, parallel to the orogen main strike, and become older towards the east (e.g. Sernageomin, 2003). The most widely exposed outcrops, and those that host the Brahma prospect, correspond to the Cenozoic belt that is comprised of variably deformed volcano-sedimentary rocks ranging in age from late Eocene to Miocene (Fig. 1b; González and Vergara, 1962; Vergara et al., 1999; Sernageomin, 2003; Cabezas et al., 2018). Younger volcano-sedimentary sequences and numerous Cenozoic intrusive units of variable size are also present in this area (Fig. 1b). All these Cenozoic igneous series and their intrusive counterparts are related to arc activity lasting from at least 36 to 6 Ma (e.g. Vergara et al., 1999; Spikings et al., 2008; Astaburuaga, 2014; Cabezas et al., 2018). Outcrops of Late Cretaceous plutons are also present in the area and have been identified through radiometric determinations (Nelson et al., 1999; Spikings et al., 2008; Cabezas et al., 2018). The Brahma prospect is emplaced in the westernmost part of the Cenozoic belt that dominates the western Principal Cordillera. The hosting unit corresponds to the Colbún Formation (~35 to 36°S; Karzulovic et al., 1972), a volcanic and minor sedimentary continental series with an average thickness of 1900 m (González and Vergara, 1962) and a late Eocene to middle Miocene age (~35 to 15 Ma; Vergara et al., 1999). Immediately to the east of the prospect location, the El Melado Pluton constitutes the main intrusive unit present in the area. It corresponds to a hornblende granodiorite showing both Miocene and Late Cretaceous ages (Nelson et al., 1999, Spikings et al., 2008; Cabezas et al., 2018), respectively restricted to the eastern and western portions of the unit.

In this region, the Cenozoic evolution that the above mentioned units represent is poorly constrained. However, these form part of an (Eocene?) Oligocene-Miocene magmatic belt that can be followed continuously to the north at least up to ~ 33°S, an area hosting highly endowed Miocene porphyry deposits. Here, the overall evolution is dominated by the early development of an Oligocene-Miocene intra-arc subsiding and extensive basin, the so called Abanico Basin, inverted in the early Miocene (e.g. Charrier et al., 2002, 2007). From then onwards such region was subjected to continuous compression which has proceeded along with the crustal thickening and uplifting processes responsible for the configuration of the current Andean orogen (e.g. Charrier et al., 2002, 2007; Giambiagi and Ramos, 2002; Farías et al., 2010). This period encompasses the formation of the giant porphyry copper deposits that comprise the Miocene metallogenic belt between 32°-34°S (Fig. 1a): (i) Los Pelambres-El Pachón (31°43′S), (ii) Rio Blanco-Los Bronces (33°08′S), and (iii) El Teniente (34°04′S). All these show a wide range of Miocene-Pliocene ages for their associated magmatic and hydrothermal activity, but the main mineralizing events have been bracketed between ~ 12–9 Ma for the northern one (Bertens et al., 2003, 2006) and between ~ 7–5 Ma for the two southerly ones (e.g. Deckart et al., 2005, 2014; Maksaev et al., 2004).

2.2. Metallogenic background

The crosscutting relationships of the Brahma prospect suggest it formed from a Neogene mineralizing event. This prospect however does not formally belong to the Miocene-Pliocene metallogenic belt of the margin whose termination is at ~ 34°S (location of El Teniente deposit; e.g. Camus, 2003; Maksaev et al., 2004, 2007). Further south, roughly along the same belt, a series of Miocene deposits and prospects have been recognized (Fig. 1a), but their full economic and metallogenic potential remain unknown. The Cu-Mo deposits of this belt are typically related to multi-phase porphyritic stocks and are associated with magmatic-hydrothermal breccia complexes (e.g. Camus, 2003; Maksaev et al., 2007). At a regional scale, their intrusive units vary from plutonic to hypabyssal bodies corresponding to the pre-, syn- and post-mineralization units and show ages between 21.6 and 4.6 Ma (e.g. Camus, 2003; Bertens et al., 2003, 2006; Maksaev et al., 2004, 2007; Deckart et al., 2013, 2014; Muñoz, 2008). Although this porphyry belt runs subparallel to the main strike of the Andean orogen, the associated structural control is not evident and no exposed regional scale structures can be related to the deposits distribution (e.g. Camus, 2003; Maksaev et al., 2007). However, at local scales in each deposit, different sets of structures have been recognized controlling the emplacement and evolution of the porphyry Cu systems (for a review see Camus, 2003).

Up to date, only minor exploration and informal mining activities have been developed in some areas near the Brahma prospect. These correspond to the Austral porphyry prospect, located about 9 km to the northeast, and the Ancoa, Teatinos, Calabozos and Roblería targets (Fig. 1b). The mineralization in the Austral prospect and all the targets corresponds to pyrite and less chalcopyrite mostly associated with quartz stockwork veins hosted in hydrothermal breccias and granodioritic bodies cut by porphyritic dikes of andesitic and rhyodacitic composition (Sanchez and Motta, 2013). Particularly, the Austral prospect and the Ancoa target show in addition secondary Cu oxidized minerals such as chrysocolla and malachite. All the hydrothermal systems described above are controlled by structures of NW-SE, NS and subordinately NE-SW directions (Burns et al., 2008; Sanchez and Motta, 2013).

3. Sampling and analytical procedures

All samples collected for geochronology in this study were taken from drill cores recovered from boreholes BRA002, BRA003, BRA004 and BRA006, these represented on the cross-section A-A' (Fig. 2). In addition, samples from the BRA005 and BRA007 boreholes were also collected for geochemical analyses (Fig. 2a).

3.1. U-Pb geochronology and Hf isotopic determinations

U-Pb geochronological determinations were performed in-situ in single zircon crystals in five samples belonging to the main intrusive units identified in the Brahma prospect (Supplementary Material Item 1; Fig. 2). The same crystals were then used for determination of Hf isotopic concentrations (Supplementary Material Item 2). Both analyses were performed by the laser ablation method at the Centro de Geociencias - Universidad Autónoma de México (UNAM), Mexico. Zircon grains were first separated from total rock samples using standard crushing, washing, heavy liquid, and paramagnetic procedures.

U-Pb analyses were performed employing a Thermo ICap Qc quadrupole ICP-MS coupled with a Resolution M050 excimer laser workstation. U and Th concentrations were calculated employing external standard zircons, 91,500 (1065.4 ± 0.6 Ma; Wiedenbeck et al., 1995) and Plešovice (337.13 ± 0.37 Ma; Sláma et al., 2008), as in
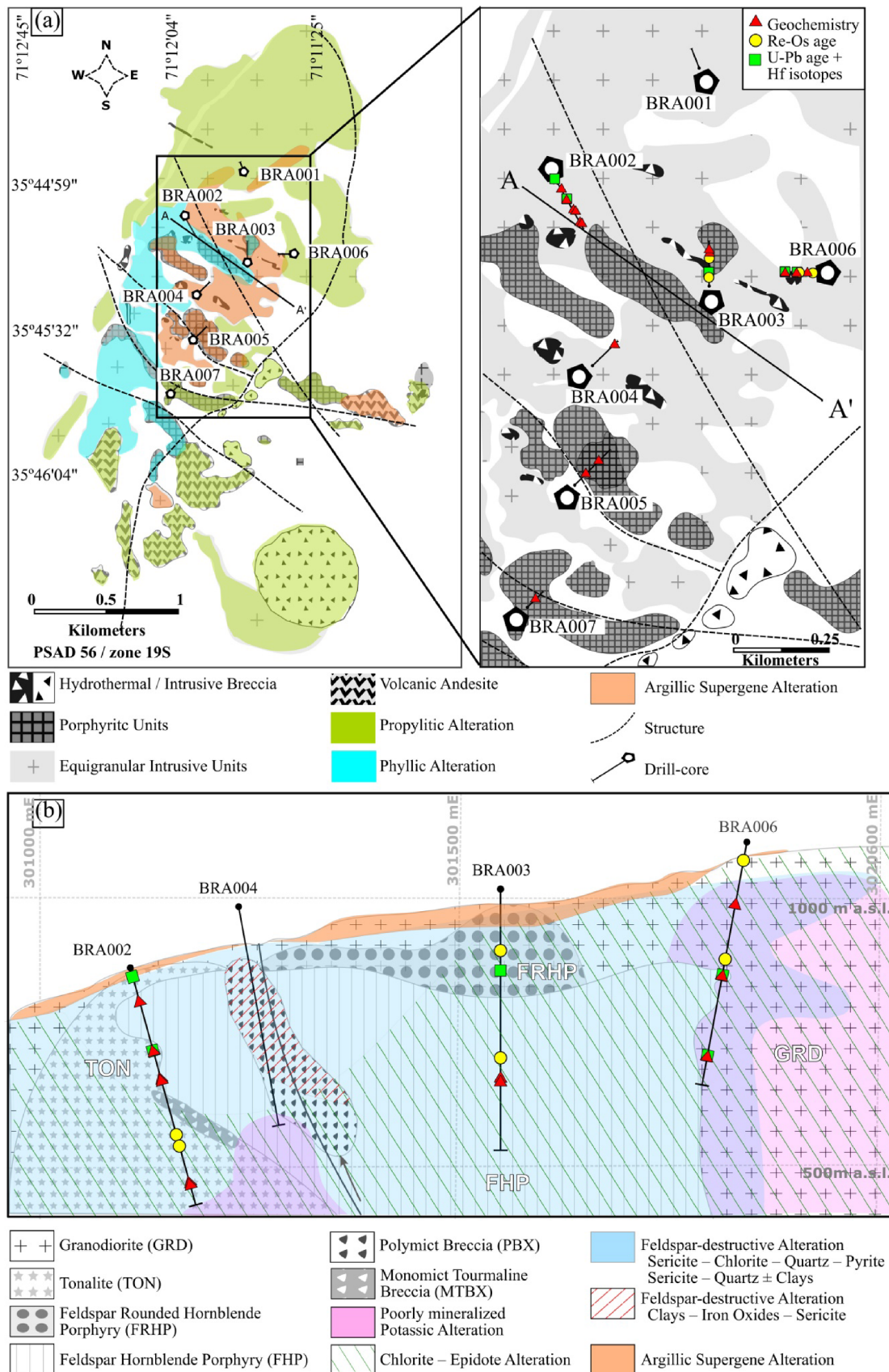
Fig. 2. Local geology of the Brahma Prospect. The symbols (red triangles, yellow circles and green squares) show the location of all samples with geochemical and geochronological determinations. (a) Geologic map of the Brahma prospect according to Burns et al. (2008). The map shows the location of 7 diamond drill holes and the section line A-A'. The map on the right shows a zoom of the central area of the map on the left. (b) Geologic cross section along the A-A' line (this study). The lithology and alteration is based on the mapping of the boreholes BRA002, BRA004, BRA003 and BRA006.

Paton et al. (2010). The isotopic ratios, ages and errors were calculated according to Petrus and Kamber (2012). In the data tables analytical determinations are reported at 2σ uncertainties, which were propagated according to Paton et al. (2010). Analyzed spots were 23 μm, using an analytical protocol modified from Solari et al. (2010), and these were selected after the study of transmitted light and cathodoluminescence images. For each spot a set of trace elements were also measured, in order to monitor possible inclusions in zircon crystals, using the NIST-SRM 610 glass as a reference standard and ^{29}Si as an internal standard (15.323% assumed stoichiometric value). Ages were calculated as weighted averages for the statistically coherent population (Ludwig, 2008). The presented concordia plots, probability density plots with stacked histograms, and weighted mean $^{206}Pb/^{238}U$ age calculations were carried out using ISOPLOT/EX 4.15 (Ludwig, 2008).

Hf isotopes were determined employing a Thermo Neptune Plus multi-collector ICP-MS coupled with the mentioned laser workstation. An analytical spot of 44 μm was used, locating it in homogeneous CL zones, right on top of the previous U-Pb analytical spot to ensure that the same dated domain was assessed and thus correctly recalculating the $^{176}Hf/^{177}Hf$ ratios relative to the zircon crystallization age. The external reproducibility of standard zircon grains broadly varied by ± 1 epsilon unit. Each ablation was run for 40 s, with repetitions at 5 Hz rate and an energy density of 6 J/cm^2. The isobaric interferences of ^{176}Lu and ^{176}Yb on the ^{176}Hf signal were corrected by monitoring ^{175}Lu, ^{172}Yb and ^{173}Yb and applying independent mass bias corrections as described in Solari et al. (2018).

3.2. Re-Os geochronology

Re-Os geochronological determinations were performed on six samples containing molybdenite (Fig. 2). Analyzed samples were carefully selected after a detailed study of paragenetic vein relationships (Table 1). Mineral samples of molybdenite were crushed, hand-picked and powdered at Juniata College, United States. Since the distribution of Re and Os is heterogeneous in sulfide minerals (e.g. Freydier et al., 1997; Mathur et al., 1999; Stein et al., 2001; Barra et al., 2003), grains were collected in different places within the same domain (e.g. vein, disseminated) in order to homogenize the variability in Re-Os ratios.

For molybdenite analyses samples were collected from vein types II, V, VII and IX (Table 1). Considering that for such analyses the amount of mineral is not critical (0.1–0.05 g), samples for each one of the molybdenite bearing veins were considered, including the fine ones (~1 mm), and also from disseminated mineralization. The alteration assemblages present in the sampled veins and their halos (Table 1) suggest that the molybdenite mineralization has not been disturbed by local and high temperature (> 350 °C) subsequent hydrothermal events. No clay inclusions were found in molybdenite grains that could give erroneously young ages due to an excess of Re (Ruiz and Mathur, 1999).

For performing the analyses approximately 0.04–06 gr of each molybdenite sample was loaded in a Carius tube. Spikes of ^{185}Re and ^{190}Os were added along with 3 ml of aqua regia following the procedure described in Shirey and Walker (1995). About 1 ml of H_2O_2 was added to the acid mixture to ensure the complete oxidation of the samples and spike equilibration (Shirey and Walker, 1995; Frei et al., 1998; Mathur et al., 2000). The tubes were placed in a stainless-steel jacket and heated overnight in an oven at 180–220 °C. The Carius tube solution was later treated in a two-stage distillation process for Os separation similar to that described by Shirey and Walker (1995) and Frei et al. (1998). Os was further purified using a microdistillation technique (Birck et al., 1997) and then loaded on a platinum filament with Ba(OH)$_2$ to enhance ionization. The Re that remains in solution of the first distillation was extracted and purified through a two-stage ion exchange chromatography process. Finally, Re was loaded on a nickel filament. All the samples were analyzed by negative thermal ion mass spectrometry

(NTIMS; Creaser et al., 1991), a VG 54 mass spectrometer at the University of Arizona.

3.3. Whole rock geochemical analyses

For chemical whole rock analyses, samples were crushed in a reciprocating steel crusher and subsequently reduced to the powder used for analyzing major and trace elements (15 samples; Fig. 2). Analyses were performed at Activation Laboratories, Ontario - Canada, by the procedure 4Litho (www.actlabs.com), which respectively combines ICP-OES and ICP-MS techniques for geochemical determinations. Samples were fused by lithium metaborate/tetraborate and lately diluted for analyses in a Perkin Elmer Sciex ELAN 6000, 6100 or 9000 ICP-MS. Three blanks and five controls (three before sample group and two after) were analyzed per group of samples, duplicates were fused and analyzed every 15 samples, and the instrument was recalibrated every 40 samples. Data quality was controlled by running several standards, relative standard deviations are generally ≤ 5%, and the detection limits are indicated in Table 4.

4. Results

4.1. Geology of the deposit

The Brahma prospect covers an area of around 62 km^2 and was discovered through a geochemical stream sediment study. There are only a few previous studies performed on this prospect, all of which are exploration technical reports (Culbert, 2007; Burns et al., 2008; Sanchez and Motta, 2013). In this study a lithologic and alteration cross-section was constructed from observations made during detailed logging of drill cores from four boreholes (BRA002, BRA003, BRA004, and BRA006) supplemented by information from previous studies (Fig. 2a, 2b). Most of the material collected for our analytical campaign were sampled from drill cores recovered from the boreholes depicted on the cross-section A-A' (Fig. 2b) and a minor group of samples for geochemical analyses were also collected from the remaining drill cores (Fig. 2a).

Overall, the geology of the Brahma prospect is dominated by a granodioritic unit that hosts numerous smaller porphyritic intrusives and breccia bodies (Fig. 2a). For the area, a series of NW striking structures are dominant and these are in turn crosscut by a main NE striking structure (Fig. 2a; Burns et al., 2008). The mineralization and alteration are mainly hosted by the intrusive units (Fig. 2b). A wide and well-developed zone of feldspar destructive (phyllic ± argillic) alteration is recognized, which has locally been overprinted by supergene argillic alteration (clays, limonites, and dominant hematite) with an intense stockwork of quartz-limonite (Fig. 2a; Burns et al., 2008; Sanchez and Motta, 2013). Towards the outer limits of the prospect, propylitic alteration predominates and extends for several kilometers (Burns et al., 2008). This alteration is characterized by an epidote-chlorite-calcite-pyrite assemblage with stockworks of quartz–chlorite–pyrite–chalcopyrite in the vicinities of the phyllic center (Burns et al., 2008).

4.1.1. Lithology

A total of six main lithologic units are recognized within the Brahma prospect. These include two equigranular intrusives, two porphyritic intrusives, and two hydrothermal breccia units (Table 2; Fig. 2b).

(1) Granodiorite Unit (GRD)

According to crosscutting relationships the oldest unit is a granodiorite, which has a widespread distribution (Fig. 2b). It is characterized by a phaneritic, equigranular and hypidiomorphic texture showing a homogeneous structure and isotropic fabric (Fig. 3a). It is leucocratic to mesocratic with a 25% volume of mafic minerals. The main mineral phases are plagioclase (50%), quartz (15%), alkali feldspar (10%), hornblende (15%) and biotite (10%). Grain sizes are variable ranging

Table 1
Summary of the main vein types and their characteristics identified in the Brahma prospect study.

Vein type	Mineralogy	Halo mineralogy	Shape and dimensions	Alteration
I	Bt	Without halo	Thin veins, of up to 0.25 cm in width and irregular shape.	Potassic
II	Qtz – Kfs ± (Py – Ccp – Mo)	Kfs ± Ab	Straight veins with fairly regular borders and widths of 1 to 3 cm. The halo (sometimes absent) is usually thin (1 mm) and of irregular shape.	Potassic
III	Qtz – Anh – Gp – Py	Chl – Py ± gray Ser	Slightly sinuous to straight veins with fairly regular borders and widths of 0.5 to 1.5 cm in width and dark appearance. The Py usually forms a straight but discontinuous suture.	Fspdestructive (Ser – Chl – Qtz – Py)
IV	Qtz – Anh – Gp – Py ± Sp ± Tur	Ser – Py ± Tur ± Clays	Straight veins with irregular to regular borders and widths of 0.5 to 3 cm. Halo of irregular shape of up to 2 cm in width. Some pyrites are partially replaced by sphalerite.	Fspdestructive (Ser – Qtz ± Clays)
V	Mo – Gp ± Py	Ser – Qtz ± Chl	Straight massive molybdenite veins with regular borders and widths of 0.5 to 1 cm. Halo of regular shape of up to 2 cm in width. These veins show micro-brecciation textures of the host rock in some areas.	Fspdestructive (Ser –Chl – Qtz – Py)
VI	Qtz – Gp – Anh – Chl – Py ± Ccp	Chl – Ser	Straight veins with regular to irregular borders and widths of 0.2 to 2.5 cm. Halo of irregular shape of up to 0.3 cm in width. The sulfides form a straight and continuous suture at the center of the vein.	Fspdestructive (Ser –Chl – Qtz – Py)
VII	Mo – Qtz – Ser	Without halo	Thin veins, of up to 0.15 cm in width and irregular shape.	Fspdestructive (Ser – Qtz ± Clays)
VIII	Qtz – Py – Bn – Cc ± (Gn – Sp – Ccp)	Ser – Clays	Straight veins with regular border of about 0.7 cm in width. Halo of irregular shape of up to 0.5 cm in width. The Py is partial to totally replaced by Bn, Gn and Sp, while the Bn is partially replaced by Cc. All the sulfides are forming a straight and continuous suture.	Fspdestructive (Ser – Qtz ± Clays)
IX	Chl – Ep – Py ± (Ccp – Mo)	Chl – Ser	Straight thin veins, of about 0.4 cm in width and regular borders. Halo of irregular shape of up to 0.6 cm in width. The sulfides are disseminated.	Chl –Ep
X	Py – Qtz ± Sp	Clays	Massive Py veins of straight shape and regular border. About 0.5 cm in width. The Py is partially replaced by Sp in some areas.	Fsp-destructive (Clays –Fe Oxides ± Ser)

OBS:

- Mineral abbreviations as follows. Anh: anhydrite; Bn: bornite; Cc: chalcocite; Chl: chlorite; Ccp: chalcopyrite; Ep: epidote; Gn: galena; Gp: gypsum; Kfs: K-feldspar; Mo: molybdenite; Py: pyrite; Qtz: quartz; Sp: sphalerite; Tur: tourmaline.

6

Table 2
Summary of principal characteristics of the main lithological units identified in the Brahma prospect study.

Lithologic Unit	Age ± 2σ (Ma) [MSWD]	Cross cut relations	Spatial distribution	Main components	Alteration and mineralization
Granodiorite (GRD)	14.6 ± 0.4[2.2]	Hosts all the later units in the prospect.	Wide extension (about 70% of the exposed surface). Mostly intercepted by the BRA006 borehole.	Pl (45%), Qtz (20%), Kfs (15%), Hbl (10%), Bt (10%), Mag (< 1%).	Weak early potassic alteration (represented by type I and II veins) without economic mineralization. Chl – Ep alteration superimposed. Py, Ccp and Mo disseminated and associated to IX veins.
Feldspar and Rounded Hornblende Porphyry (FRHP)	14.1 ± 0.2[1.2]	Intruding the GRD.	Little surficial expression. Interpreted in the first 200 m of the BRA003 borehole.	Phenocrysts dominated by rounded and tabular Hbl (10%), Pl (20%), Qtz and Kfs (5%).	Pervasive Fsp-destructive alteration with a weak Chl – Ep alteration superimposed. In some areas shows brecciation texture. Py with minor Ccp and Mo disseminated and filling fractures.
Tonalite (TON)	13.4 ± 0.4[0.99] 13.8 ± 0.5[1.5]	Intruding the GRD and FRHP.	Little to no surficial expression. Intercepted mainly in the last 176 m of the BRA002 borehole.	Pl (60%), Qtz (30%). The mafic phases (10%) are Bt, Hbl and Mag.	Weak Fsp-destructive alteration. Abundant Py and Sp with minor Ccp. This mineralization occurs both disseminated and associated to type IV veins. Abundant Mo disseminated and associated to type V veins with micro-brecciation characteristics.
Feldspar and hornblende porphyry (FHP)	9.3 ± 0.2[1.4]	Intruding all the previous units.	Wide distribution at subsurface levels approximately in the center of the cross section A-A'.	Phenocrysts dominated by Pl (35%), Hbl (15%), Qtz and Kfs (5% in total).	In deeper areas a Ser –Chl – Qtz – Py Fsp-destructive assemblage predominates, whereas in micro brecciated, and in shallower areas a Ser – Qtz ± Clays Fsp-destructive assemblage predominates. Abundant Py and lesser Ccp both disseminated and filling fractures. Strong Sp mineralization mostly associated to brecciated zones. This unit shows a better development of Cu mineralization compared to other ones. Occasional Mo associated to type VII veins.
Monomict tourmaline breccia (MTBX)	–	In the contact between the TON and the PFH units.	Intercepted at the middle parts of the BRA002 borehole.	Angular to sub angular shaped TON clasts cemented by Tur, Ser, Qtz and Py.	Clasts show pervasive Ser – Qtz ± Clays Fsp-destructive alteration. Disseminated Py mineralization with minor Ccp, Bn, Sp and Gn (in clasts and matrix/cement). This mineralization is also associated to type VIII veins which show a highly secondary enrichment replacement.
Polymict breccia (PBX)	–	Intruding the FHP.	Intercepted by most of the BRA004 borehole.	Sub-angular shaped PFH, minor FRHP, GRD, TON and other unidentified porphyry clasts. Fragments immersed in a rock flour, Qtz and Clays matrix and cement of Cal, Anh and Gp.	Highly pervasive Fsp-destructive alteration (Clays –Fe Oxides ± Ser). Associated to this alteration there is abundant disseminated and vein related (type X) Py mineralization, partially replaced by Sp, Gn and Cc in traces.In deeper parts of the body a Ser –Chl – Qtz – Py alteration with type VI veins predominates.

OBS:
- Listed ages correspond to zircon U-Pb determinations from this work.
- Mineral abbreviations as follows. Anh: anhydrite; Bt: biotite; Bn: bornite; Calc: calcite; Cc: chalcocite; Chl: chlorite; Ccp: chalcopyrite; Ep: epidote; Fsp: feldspar; Gn: galena; Gp: gypsum; Hbl: hornblende; Kfs: K feldspar; Mo: molybdenite; Pl: plagioclase; Py: pyrite; Qz: quartz; Sp: sphalerite; Tur: tourmaline.
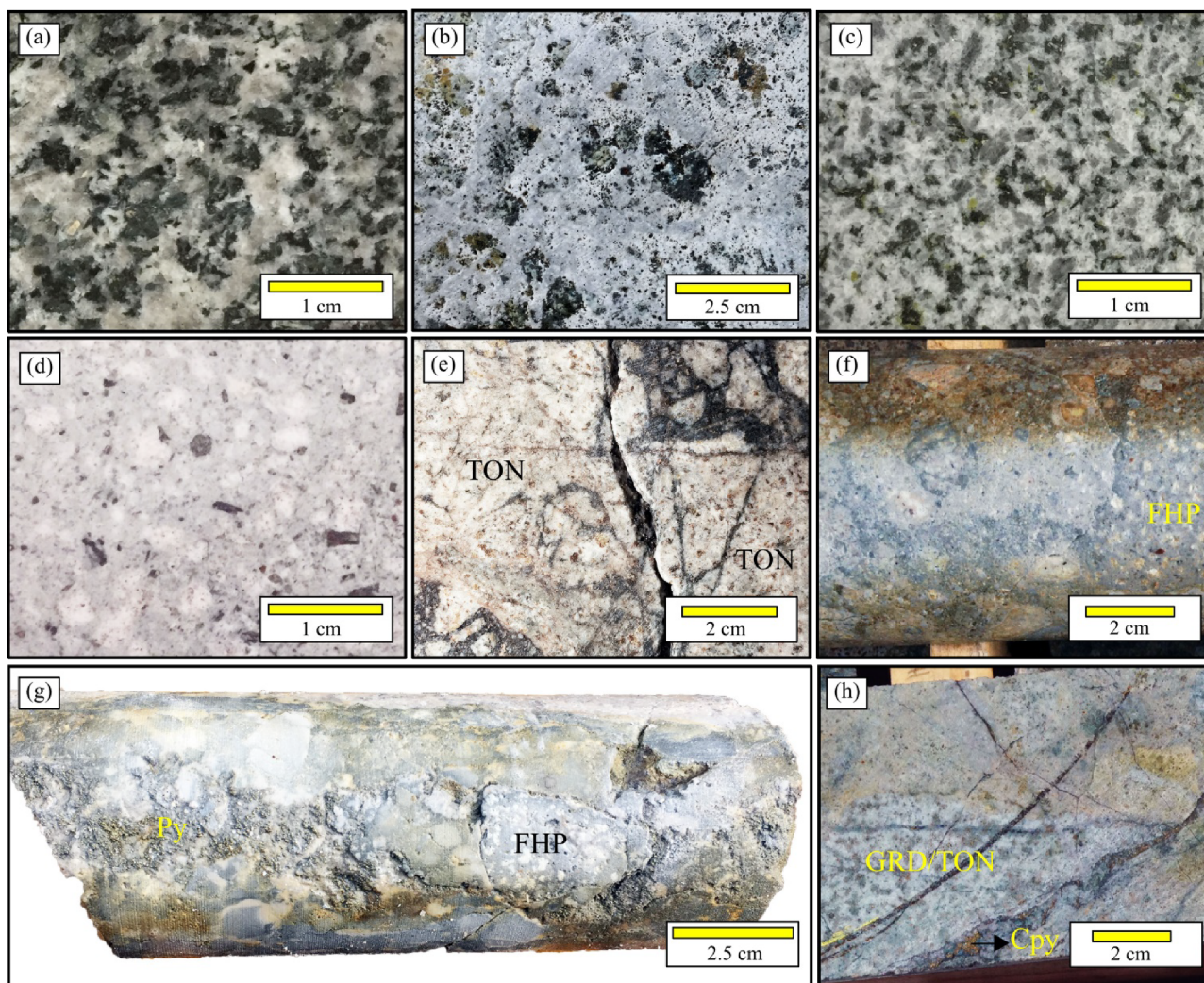
7

Fig. 3. Photographs of each lithologic unit recognized in the studied area (Fig. 2b). (a) Granodiorite (GRD). (b) Feldspar rounded hornblende porphyry (FRHP). (c) Tonalite (TON). (d) Feldspar hornblende porphyry (FHP). (e) Monomict tourmaline breccia (MTBX), with clasts of TON with a pervasive feldspar-destructive alteration. (f) Polymict breccia (PBX). (g) PBX with clasts of FHP and other undetermined intrusive units. The clasts are strongly altered by feldspar-destructive alteration. It also shows abundant rock flour matrix and cement of carbonates, gypsum, anhydrite and pyrite. (h) PBX with sericite-chlorite-quartz-pyrite alteration. Comparatively, it shows larger clasts and a more competent aspect.

mostly between 2 and 5 mm. Occasionally, particular textures shown by this rock include zonation in plagioclase crystals and a consertal texture developed by quartz, alkali feldspar and plagioclase.

(2) Feldspar and Rounded Hornblende Porphyry Unit (FRHP)

This intrusive body intrudes the GRD and has a limited distribution on section A-A' (Fig. 2b). It has an inequigranular, hipocrystalline and porphyritic texture and is leucocratic. The phenocrysts are hypidiomorphic and average 35% of the rock volume. The rock contains 10% of the hornblende grains in two populations: one composed by single tabular crystals and another forming clusters of approximately 5 to 10 mm (Fig. 3b). Such clusters, which macroscopically look like rounded hornblende grains, give a distinctive aspect to this unit that helps distinguishing it from other porphyries. It also contains 20% plagioclase (0.2 to 4 mm), and 5% of anhedral quartz and alkali feldspar (0.2 to 2 mm). The plagioclase crystals are typically zoned and show glomeroporphyritic texture. In addition, scarce plagioclase and quartz crystals are fragmented and show resorption textures. The groundmass (~65% in volume) is composed of fine-grained (< 0.1 mm) quartz and alkali feldspar, in the same proportion, showing felsitic texture and arranged in a homogeneous mosaic.

(3) Tonalite Unit (TON)

This unit occurs in the western portion of the study area and does not crop out at surface (Fig. 2b). The TON is very similar to the GRD; however it is distinguished based on it being more leucocratic, containing smaller grain sizes and having a paucity of alkali feldspar crystals (Fig. 3c). The grains are hypidiomorphic and occur in an isotropic fabric, but flow textures are locally developed in the contact with the FRHP. On average, this rock unit is composed of 60% plagioclase, 30% quartz, and 10% of mafics (biotite, hornblende and magnetite). Grain sizes are variable ranging mostly between 0.5 and 4 mm. Some plagioclase crystals are zoned. Consertal texture between quartz and some plagioclase crystals is also observed.

(4) Feldspar and Hornblende Porphyry Unit (FHP)

This intrusive unit distributes at subsurface levels approximately in the center of the study area and is cutting all the units mentioned before (Fig. 2b). It is characterized by an hypocrystalline porphyritic texture, is leucocratic and shows a homogenous and isotropic fabric (Fig. 3d). Phenocrysts are between 1 and 4 mm with an average of 35% plagioclase (2 to 8 mm), 15% hornblende (0.4 to 6 mm), and 5% of quartz and alkali feldspar (2 to 8 mm). The groundmass is composed mainly by fine grained (< 0.1 mm) quartz and alkali feldspar (44%), and minor apatite and pyrite (< 1%). Typically, the plagioclase crystals show zonation and have formed glomerocrysts in clusters up to 5 mm. This texture is more common in the FHP compared to the FRHP. Some plagioclase

and quartz crystals are fragmented and show resorption textures.

(5) Hydrothermal Breccias (MTBX, PBX)

In addition to the intrusive units, at least two hydrothermal breccia bodies were observed in the prospect. The first one occurs at the contact between the TON and FHP units (Fig. 2b) and corresponds to a monomict clast-supported breccia, with sub-angular TON fragments, immersed in a matrix of rock flour and abundant cement of tourmaline, sericite, quartz and pyrite (henceforth called MTBX: monomict tourmaline breccia) (Fig. 3e). Fragments vary in size from 5 mm to 15 cm. The second breccia body has a broader expression in the study area, in particular occurring in most of the BRA004 drill core which is dominated by a fault zone (Fig. 2b). It is a polymict clast-supported breccia with sub-angular fragments of 5 mm up to 10 cm in size (henceforth called PBX: polymict breccia; Fig. 3f-h). Due to pervasive alteration it is difficult to identify the protolith of the clasts present in this breccia body; however, FHP, FRHP and GRD/TON fragments have been recognized in addition to fragments from an unidentified porphyry (Fig. 3g, h). The clasts are immersed in a matrix of rock flour, quartz and clays, cemented by an assemblage of calcite, anhydrite and gypsum filling previous porosity. In contrast with the MTBX, the PBX body is highly friable. The latter characteristic progressively diminishes towards the deeper parts where the PBX becomes more competent and the clast sizes become larger (up to 15 cm; Fig. 3h).

4.1.2. Alteration and mineralization

Mineralization as evidenced in drill cores occurs as disseminations and vein infill, where it consists of pyrite, sphalerite, chalcopyrite, molybdenite, and minor galena, bornite and secondary chalcocite. The intercepted Cu mineralization is low grade reaching up to 0.24% Cu (8 m; BRA001), 0.21% Cu (14 m; BRA003), 0.14% Cu (184 m; BRA003 e) and 0.19% Cu (32 m; BRA004), however, some shorter intercepts reach 0.5 to 1% Cu (Burns et al., 2008). Regarding Mo mineralization, the best intercepts have average grades of 0.02% (20 m; BRA006) and 0.01% (46 m, 16 m and 14 m; BRA002, BRA003 and BRA001, respectively), reaching values of up to 0.07 to 0.1% in shorter intercepts (Burns et al., 2008). Based on drill core logging (Table 1; Figs. 4, 5), the alteration and mineralization paragenesis determined in this study is described as follows.

(1) Potassic Alteration

This alteration is scarce within the studied area and was mainly intercepted in BRA006 (Fig. 2b) and the last few meters of BRA002 and BRA004. It is characterized by a slight replacement of mafic minerals by secondary biotite and the occurrence of thin biotite veins (these mostly chloritized; type I) crosscut by thick quartz ± K–feldspar veins (type II) (Table 1; Fig. 5a, b and 6b). Type II veins locally have patches of chalcopyrite and molybdenite mineralization. The potassic alteration is obscured by an overprinting and pervasive feldspar-destructive

alteration. Overall the abundance of the copper and molybdenum mineralization associated with this early alteration stage is scarce.

(2) Feldspar-destructive Alteration

Feldspar-destructive alteration (Yang et al., 2009), equivalent to phyllic ± argillic alteration (sensu Corbett and Leach, 1998), is the most abundant and well-developed in the prospect area. This alteration varies from an incipient replacement of feldspar and mafic minerals to sericite and/or clay minerals (as defined in Corbett and Leach, 1998; sericitic alteration as defined by Sillitoe, 2010), to complete obliteration of the igneous textures by pervasive alteration to the same alteration assemblage. In the deeper zones this alteration is characterized by a sericite–chlorite–quartz–pyrite alteration assemblage with thick veins of molybdenite–gypsum ± pyrite (type V) (Table 1; Fig. 5e) and veins of quartz–gypsum–anhydrite–pyrite ± chlorite ± chalcopyrite with chlorite and sericite haloes (type III and VI) (Table 1; Fig. 5c, f). At shallow depths it is characterized by a sericite–quartz ± clays alteration assemblage. Associated with the sericite–quartz ± clays alteration assemblage, there are veins composed of quartz–anhydrite–gypsum–pyrite ± sphalerite ± tourmaline (type IV) (Table 1; Fig. 5d) and veins of molybdenite–quartz–sericite (type VII) (Table 1; Fig. 5g).

Strong feldspar-destructive alteration occurs preferably at the PBX breccia, where the clasts are almost totally replaced by low birefringent clays (probably kaolinite), iron oxides like rutile and hematite, and minor sericite (Fig. 6a). Associated to such alteration assemblage, there is abundant pyrite mineralization that occurs both as disseminations (in clasts and matrix) and as veins (type X) (Table 1; Fig. 5j), pyrite minerals partially to totally replaced by sphalerite and galena in some areas (Fig. 5j, k). Overall, igneous textures are poorly preserved. This clays–iron oxides–sericite alteration dominates in most of the PBX breccia body; however, in depth the dominant alteration assemblage corresponds to sericite–chlorite–quartz–pyrite (Fig. 3h).

(3) Chlorite-Epidote Alteration

Chlorite-epidote alteration (propylitic as defined by Corbett and Leach, 1998; Sillitoe, 2010) is mainly intercepted in BRA006 within the GRD (Fig. 2b). This alteration is weakly pervasive and it is characterized by epidote alteration of plagioclase and a selective substitution of primary biotite and hornblende by chlorite, epidote, pyrite and magnetite. In addition, there are also chlorite–epidote veins containing molybdenite-chalcopyrite and pyrite patches (type IX) (Table 1; Fig. 5i) associated to this alteration type. Type IX veins crosscut type II veins (Fig. 6b), however, there is a lack of clear crosscutting relationships with the rest of the veins. Some type IX veins show thick haloes of sericite ± clays (Fig. 6c), suggesting that chlorite–epidote alteration may have formed simultaneously with feldspar-destructive alteration.

(5) Supergene Alteration and Mineralization

Supergene argillic alteration is associated with the leached cap and

Vein Type	Mineralogy	Early	Late	Supergene	Alteration
I	Bt	▬▬▬			Potassic
II	Qtz –Kfs ± (Py – Ccp – Mo)	▬▬▬			Potassic
III	Qtz – Anh – Gp – Py		▬▬▬		Fsp-destructive (Ser – Chl – Qtz – Py)
IV	Qtz – Anh – Gp – Py ± Sp ± Tur		▬▬		Fsp-destructive (Ser – Qtz ± Clays)
V	Mo – Gp ± Py		▬▬		Fsp-destructive (Ser – Chl – Qtz – Py)
VI	Qtz – Gp – Anh – Chl – Py ± Ccp		▬▬		Fsp-destructive (Ser – Chl – Qtz – Py)
VII	Mo – Qtz – Ser		▬▬		Fsp-destructive (Ser – Qtz ± Clays)
VIII	Qtz – Py – Bn – Cc ± (Gn – Sp – Ccp)		▬▬ ▪ ▪ ▪		Fsp-destructive (Ser – Qtz ± Clays)
IX	Chl – Ep – Py ± (Ccp – Mo)		▬▬		Chl – Ep
X	Py – Qtz ± Sp		▬▬ ▪		Fsp-destructive (Clays – Fe Oxides ± Ser)

Fig. 4. Summary of vein paragenesis in the Brahma prospect. The relative timing of each vein was determined by observed crosscutting relationships. Vein types I and II correspond to early mineralization, vein type III corresponds to a transitional mineralization stage and vein types IV to X are related to late stage mineralization. Vein types VIII and X show supergene sulfide replacement. Mineral abbreviations as follows. Anh: anhydrite; Bt: biotite; Bn: bornite; Cc: chalcocite; Chl: chlorite; Ccp: chalcopyrite; Ep: epidote; Fsp: feldspar; Gn: galena; Gp: gypsum; Kfs: K-feldspar; Mo: molybdenite; Py: pyrite; Qtz: quartz; Sp: sphalerite; Tur: tourmaline.
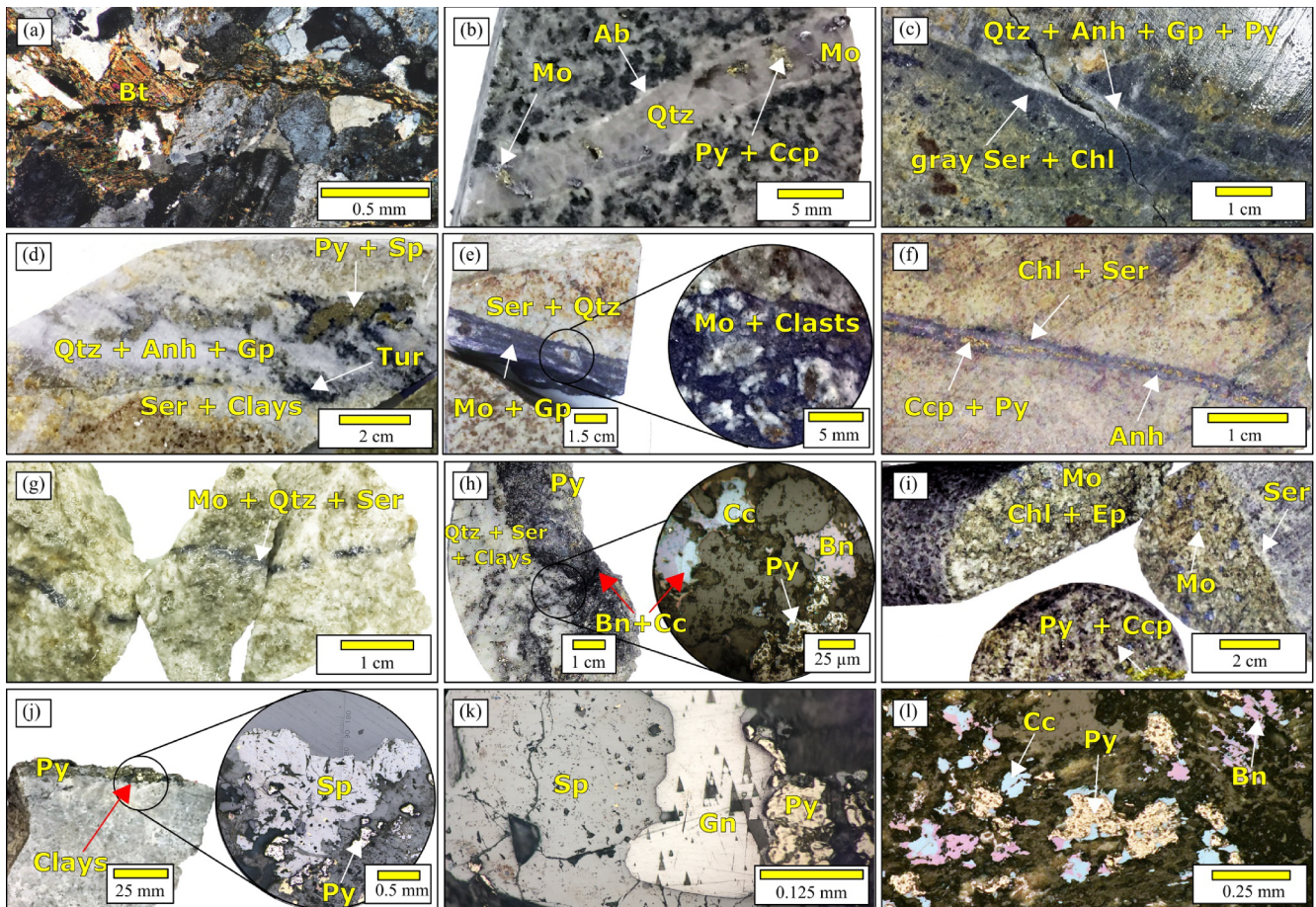
Fig. 5. Examples of each vein type recognized in the Brahma prospect. Mineral abbreviations are the same as in Fig. 4. (a) Cross polarized light photomicrograph of an early mineralization biotite vein (type I) showing irregular borders. (b) Early mineralization quartz vein (type II) with molybdenite, pyrite and chalcopyrite mineralization. (c) Vein type III showing a semi continuous pyrite suture, and irregular gray sericite + chlorite halo with a dark aspect. (d) Thick vein type IV with irregular halo of sericite and clays. (e) Thick massive molybdenite and minor gypsum vein (type V; left) showing regular borders and microbrecciation of the host rock in some areas (right). (f) Vein type VI showing a continue chalcopyrite and pyrite suture. (g) Thin molybdenite vein (type VII). (h) Quartz–sulfide vein (left) with replacement of secondary chalcocite (right; Reflected light photomicrograph in the same sample). (i) Fractures filled with epidote, chlorite and patches of molybdenite, pyrite and chalcopyrite (vein type IX). Thin sericite halo. (j) Vein type X. Fracture filled with subhedral pyrite (left) which shows partial to total replacement of sphalerite (right; Reflected light photomicrograph in the same sample). (k) Reflected light photomicrograph of a euhedral pyrite partially replaced by sphalerite and galena. (l) Reflected light photomicrograph of disseminated pyrite partial to totally replaced by bornite and chalcocite.

mainly comprises the first few meters below surface (see A-A' cross-section in Fig. 2b). Its development at depth depends on the permeability of the host rock, which is in turn directly related to the intensity of older alteration. In BRA003 and BRA004 the rocks have a pervasive feldspar-destructive alteration and the leached cap reaches between 18 and 40 m from surface, while in BRA002 and BRA006 the leached cap only reaches between 12 and 18 m (Fig. 2b) given the presence of less altered and more competent rocks. This alteration is characterized by abundant clays, limonite and pyrite box works. Jarosite is dominant at surface and characterized by giving an orange appearance. In the deepest areas, hematite and goethite associated with fractures predominate.

Supergene mineralization is scarce within the profile depicted in the A-A' cross-section. It is characterized by the presence of secondary enrichment Cu sulfides, mainly chalcocite partially replacing bornite, chalcopyrite and pyrite in a lesser degree (Fig. 5h, l). There are also traces of covellite replacing chalcocite and bornite micro-inclusions in pyrite. In general, secondary enrichment is irregular and poorly developed, occurs through fractures and is associated with areas of greater permeability, thus it is not found in the GRD and is comparatively more abundant in fault zones, highly altered rocks, and breccia units. The best development of supergene mineralization is represented in the type VIII veins, which are composed of quartz–sericite–pyrite–galena–sphalerite ± chalcopyrite partially coated

by bornite and secondary enrichment chalcocite and covellite (Table 1; Fig. 5h). These veins cut the monomict tourmaline breccia body in a highly fragmented area that most probably corresponds to a fault zone.

4.2. Geochronology

4.2.1. Primary mineral determinations: U-Pb in zircon crystals

Five U-Pb geochronological determinations were performed in primary zircon crystals from the main intrusive units identified in the Brahma prospect (Table 2, Supplementary Material Item 1). Analyzed samples distribute along the full section studied in this work and were collected from drill cores of different levels of the BRA002, BRA003 and BRA006 boreholes (Fig. 2). One determination was performed for each unit except for the unit TON for which two samples were analyzed. This was done to check if the slight variations in mineralogical and textural features observed along the BRA002 corresponded to the same unit.

The oldest primary ages obtained are recorded by the units GRD and the FRHP (Table 2). For these, coherent populations with nearly unimodal distributions indicate weighted average ages of respectively 14.6 ± 0.4 Ma (MSWD = 2.2; all errors reported at 2σ) and 14.1 ± 0.2 Ma (MSWD = 1.2; Fig. 7). In addition, results for both units also show scarce ages of around 17 Ma (Fig. 7) which records the presence of older inherited material. The slightly older age of the GRD
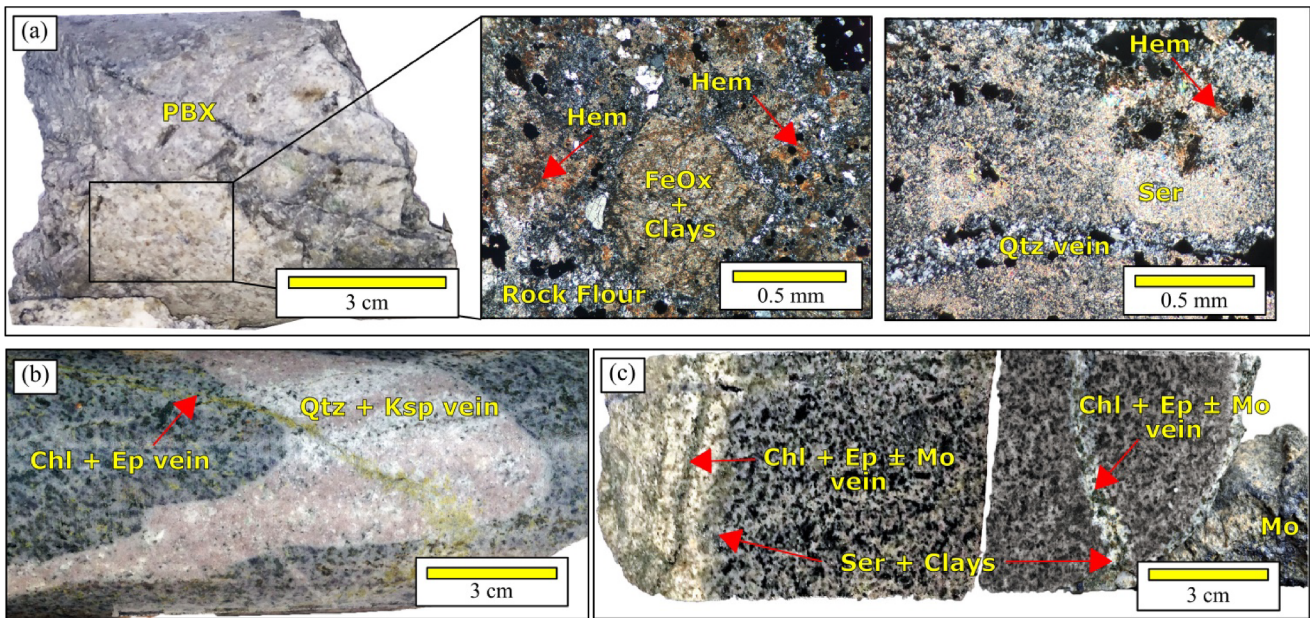
Fig. 6. (a) PBX (Polymict Breccia) with clays–iron oxides–sericite feldspar-destructive alteration. Hand sample (left) and two cross polarized light photomicrographs of the same sample (right). (b) Potassic alteration vein type II cut by a type IX chlorite–epidote alteration vein. (c) Type IX chlorite–epidote vein showing a halo of sericite and clays. Mineral abbreviations are the same as in Fig. 4.

respect to that of the FRHP is consistent with the cross-cut relations observed in the Brahma prospect, where the former hosts all the later intrusions identified. However, ages obtained for both units are indistinguishable within error thus indicating that they correspond to mostly coeval intrusive pulses. Following in age, U-Pb determinations were performed on two samples of the TON (Table 2). For one sample
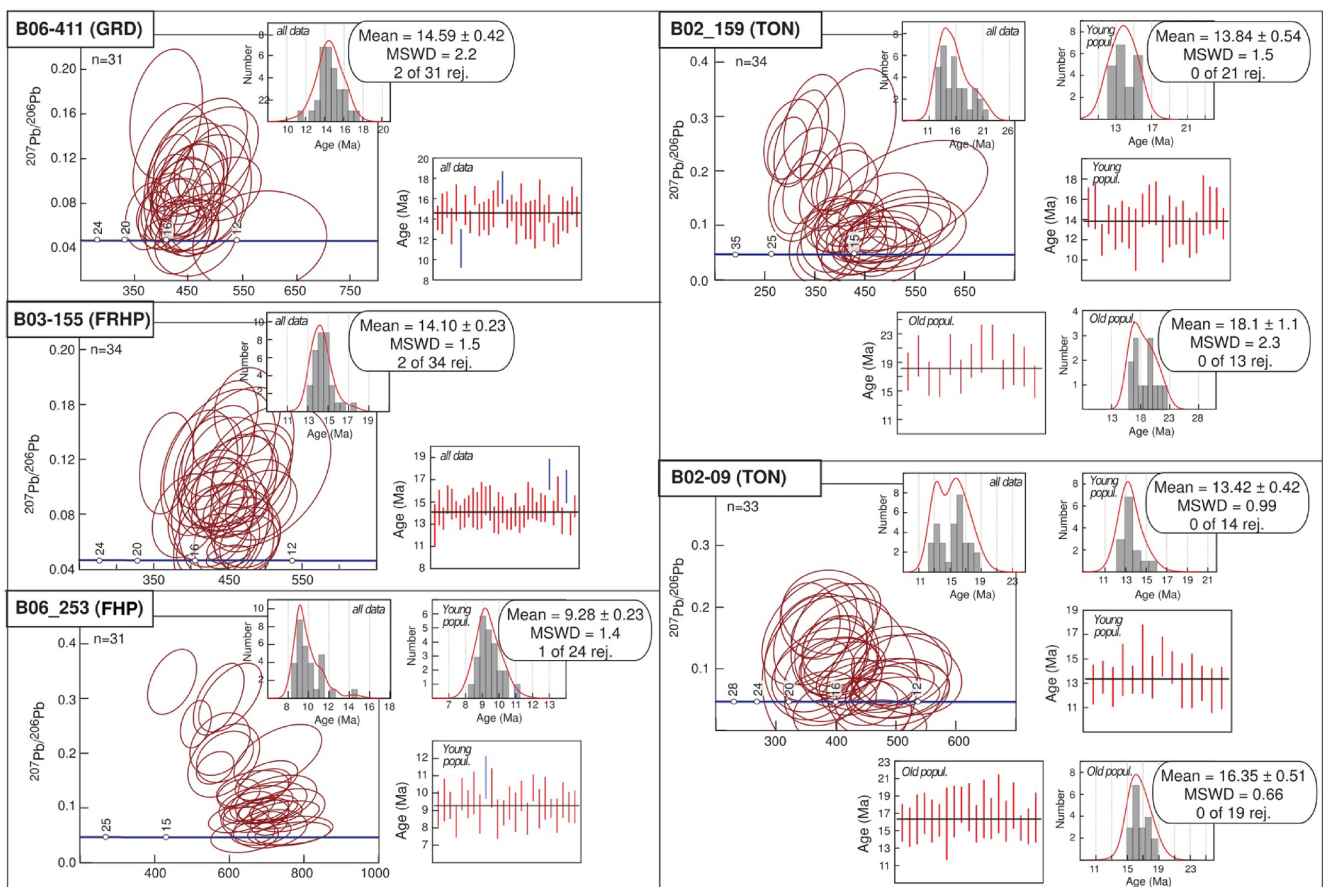

Fig. 7. U-Pb age determinations in primary zircons of igneous units from the Brahma prospect. Tera-Wasserburg plots, frequency histograms, probability density plots and weighted average diagrams are presented. In all panels, errors are considered at 2σ level. Abbreviations correspond to rej.: rejected; popul.: population.

(B02-09) an apparent bimodal distribution is described by the full data range obtained and this can be decomposed in two unimodal age populations with weighted average ages of 16.4 ± 0.5 Ma (MSWD = 0.66) and 13.4 ± 0.4 Ma (MSWD = 0.99; Fig. 7). For the second sample (B02_159) the full data range obtained describes an apparently mixed distribution which can be also decomposed in two unimodal age distributions with weighted averages of 18.1 ± 1.1 Ma (MSWD = 2.3) and 13.8 ± 0.5 Ma (MSWD = 1.5; Fig. 7). Two major observations must be highlighted from these results, first that the young and old age populations obtained in both samples agree within error and second that the old age populations coincide with the ~ 17 Ma inherited material recorded also by the units GRD and FRHP (Fig. 7). The youngest unit analyzed corresponds to the FHP, for which a coherent age population with nearly unimodal distribution indicates a weighted average of 9.3 ± 0.2 Ma (MSWD = 1.4; Fig. 7).

In summary, the results obtained from zircon U-Pb determinations indicate ages between ~ 9–14 Ma for the different intrusive units and they also record the presence of an inherited component of around ~ 17 Ma (Fig. 7). This assigns the magmatism present in the Brahma prospect to the middle Miocene which is consistent with the presence in this region of larger intrusive units of that age such as the El Melado Batholith (Fig. 1.b). The latter crops out ~ 2.6 km immediately to the east of the prospect location and ages between ~ 23.8 and 14.2 Ma have been reported for its Cenozoic portion (Drake et al., 1982; Nelson et al., 1999; Spikings et al., 2008; Cabezas et al., 2018). In addition, given the short time difference between the oldest units present in the prospect and the age of the inherited material, this region seems to have hosted fairly continuous magmatism at least between 17 and 9 Ma.

4.2.2. Primary mineralization determinations: Re-Os in molybdenite

A total of 6 Re-Os geochronological analyses were performed on molybdenite from each type of molybdenite bearing veins (II, V, VII and IX; Table 3) and from disseminated mineralization. In this way, early to late primary mineralization was considered for age determinations. The samples were collected from drill cores recovered from the boreholes BRA002, BRA003, and BRA006, represented on the cross-section A-A' (Fig. 2b). Unlike other sulfides, molybdenite does not incorporate initial ^{187}Os in its structure so a model age can be calculated from a single sample with the equation: t = (1/λ) ln(1 + ^{187}Os/^{187}Re), where λ is de decay constant of ^{187}Re, 1.666 × 10^{-11} ± 0.31 yr^{-1} (Smoliar et al., 1996). The uncertainties for the ages were calculated using error propagation, taking in consideration errors from spike calibrations, the uncertainty in the Re decay constant, and analytical errors. Blank corrections are insignificant for molybdenite.

Six Re-Os molybdenite age determinations gave a restricted range of dates from approximately 14 to 10 Ma, and these ages can be grouped in three: ~14, ~12 and ~ 10 Ma (Table 3). They correspond respectively to the following results: (i) 14.0 ± 0.07 and 13.9 ± 0.07 for vein type II and disseminated mineralization respectively, (ii) 12.4 ± 0.07 and 12.1 ± 0.07 for veins type V, and (iv) 10.14 ± 0.06 and 9.99 ± 0.05 for molybdenite hosted by veins type IX and VII.

Stein et al. (2001) and Selby and Creaser (2004) point out that Re-Os ages obtained by Carius tube dissolution and NTIMS analysis are highly reproducible and successful dating depends on proper

preparation of the mineral, specifically related to the grain size and amount of sample analyzed (aliquant). Molybdenite from samples B06038-1, B03310-2, B06221-3 (veins type II, VII and IX respectively; Table 3) were collected from thin veins which widths vary from 1.5 mm to 4 mm and grain sizes from 0.25 mm to 1.5 mm. Molybdenite from sample B03111-5 was collected from disseminated mineralization, and the grain size does not exceed 3 mm. On the other hand, molybdenite from samples B02315-7 and B02334-2 were collected from thick veins (10 to 20 mm of width; vein type V; Table. 3); however, the grain size does not exceed 1 mm. According to Selby and Creaser (2004), for coarse grain molybdenite (3 mm to 1.5 cm and larger) a greater amount of sample aliquant (> 0.04 g) is needed to avoid Re-^{187}Os decoupling and to obtain reproducible ages, while for fine grain molybdenite reproducible ages can be determined from samples with aliquant as little as 0.001 g. Therefore, even though all the samples could be considered as fine-grained, an aliquant of 0.05 g (for each sample) was measured in order to obtain precise and accurate ages. In addition to the above mentioned observations, all the Re-Os ages are not only relatively well correlated with the U-Pb age determinations, they are also are geologically coherent in terms of crosscut relationships of the different types of veins (Fig. 4). The early potassic sample (type II vein) records the oldest mineralization age (~14 Ma), and the sericite–quartz ± clays feldspar-destructive alteration vein (type VII) records the youngest (~10 Ma).

4.3. Geochemistry of igneous units

Whole rock geochemical analyses were performed on 15 samples from the four main intrusive units of the Brahma prospect (Table 4), these from the BRA003, BRA004, BRA005, BRA006 and BRA007 boreholes (Fig. 2). Analyzed samples were selected after a petrographic study by standard optical microscopic techniques and they correspond to the least altered specimens. This is partly evidenced by LOI values < 3.5% for 12 samples, while the remaining three show values of this parameter between 5.0% and 6.3% (Table 4). It has to be noted that despite the incipient hydrothermal alteration present in the analyzed samples, primary geochemical characteristics have been retained. This is supported by the coherent geochemical patterns displayed both by the Brahma prospect samples themselves and between these and other Cenozoic igneous units present in the nearby localities (see the following). For the 5 samples with U-Pb geochronological determinations, Hf isotopic composition was also determined in-situ in the same zircon crystals previously analyzed (Supplementary Material Item 2). In the different geochemical diagrams (Figs. 8 and 9), studied samples from the Brahma prospect have been plotted along with other relevant igneous units for comparison. From nearby localities, igneous rocks from Cenozoic stratified and intrusive units of ~ 24 to 17 Ma have been considered as representative of the regional background magmatism. These include (i) part of the Abanico Formation (González and Vergara, 1962) that crops out nearly 20 km to the east (Rojas del Castillo, 2018), (ii) the upper section of the Colbún Formation cropping out nearly 15 km to the west (Vergara et al., 1999) and (iii) the Cenozoic portion of the El Melado Batholith (Rojas del Castillo, 2018). In addition, as relevant units of the Miocene-Pliocene metallogenic belt, the mineralized areas hosting the deposits of Los Pelambres (31°43′S) and El

Table 3
Results of Re-Os analyses in molybdenite from the Brahma prospect.

Sample	Vein type	Alteration	Wall rock	^{187}Re (ppm)	Re total (ppm)	^{187}Os (ppb)	Age ± 2σ (Ma)
B06038-1	II	Potassic	GRD	485.15	771.69	112.80	14.00 ± 0.07
B03111-5	Disseminated	Fsp-destructive	FRHP	147.97	235.38	33.89	13.90 ± 0.07
B02315-7	V	Fsp-destructive(Ser –Chl – Qtz – Py)	TON	33.38	53.10	6.64	12.40 ± 0.07
B02334-2	V	Fsp-destructive(Ser –Chl – Qtz – Py)	TON	53.41	84.95	10.30	12.10 ± 0.07
B06221-3	IX	Chl – Ep	GRD	1059.81	1685.76	179.18	10.14 ± 0.06
B03310-2	VII	Fsp-destructive(Ser – Qtz ± Clays)	FHP	189.32	301.15	31.03	9.99 ± 0.05

Table 4
Results of whole rock chemical analyses.

Sample	BO2_210	BO6_411	BO6_111-2	BO7_298	BO2_064	BO2_159	BO2_401	BO2-7_217	BO2_403	BO4_387	BO3_357	BO3_2.355	BO5_193	BO5_272	BO6_253	DL²
Unit[1]	GRD	GRD	GRD	GRD	TON	TON	TON	TON	FRHP	FRHP	FHP	FHP	FHP	FHP	FHP	
Classification[2]	Bt granodiorite	Bt granodiorite	Bt granodiorite	Bt-Hbl granodiorite	Hbl tonalite	Hbl tonalite	Hbl tonalite	Hbl tonalite	Bt dacitic porphyry	Hbl dacitic porphyry	Bt dacitic porphyry	Hbl dacitic porphyry	Hbl dacitic porphyry	Hbl dacitic porphyry	Hbl dacitic porphyry	
Composition[3]	A	A	D	BA	D	D	D	D	D	A	D	D	D	D	D	
UTM-N	6,039,732	6,039,536	6,039,536	6,038,613	6,039,776	6,039,747	6,039,676	6,039,731	6,039,676	6,039,342	6,039,599	6,039,598	6,038,972	6,038,991	6,039,536	
UTM-E	301,151	301,769	301,822	301,065	301,126	301,142	301,184	301,152	301,183	301,286	301,550	301,550	301,210	301,229	301,797	
Major Elements in wt.%																
SiO_2	60.42	60.51	62.26	54.23	65.76	65.19	63.83	66.85	59.68	58.20	64.46	64.00	62.90	64.03	64.22	0.01
Al_2O_3	17.31	16.90	16.48	18.31	15.93	15.65	15.82	15.02	16.50	17.24	16.82	16.36	15.63	16.59	16.59	0.01
$Fe_2O_3(T)$	6.41	6.01	5.95	7.51	4.36	5.01	4.62	4.63	5.06	4.86	4.36	4.00	3.78	5.75	4.04	0.01
MnO	0.25	0.14	0.10	0.17	0.15	0.15	0.09	0.17	0.15	0.07	0.23	0.34	0.21	0.37	0.08	0.001
MgO	2.97	2.79	2.71	4.30	1.98	1.91	2.11	1.78	1.91	1.99	1.39	1.35	1.36	1.53	1.30	0.01
CaO	6.01	5.89	5.79	8.49	4.18	4.50	4.87	4.13	4.66	5.36	4.07	4.46	4.42	3.32	3.87	0.01
Na_2O	3.91	3.78	3.84	3.45	3.64	3.76	3.96	3.68	4.34	4.85	4.50	4.62	3.22	3.78	3.88	0.01
K_2O	0.18	1.01	1.31	0.40	0.59	0.97	0.34	0.40	0.46	0.52	0.60	0.40	0.92	0.84	2.22	0.01
TiO_2	0.60	0.67	0.66	0.76	0.48	0.48	0.51	0.44	0.52	0.61	0.48	0.46	0.42	0.43	0.47	0.001
P_2O_5	0.13	0.15	0.14	0.17	0.12	0.11	0.11	0.11	0.14	0.17	0.16	0.15	0.15	0.13	0.14	0.01
LOI	2.06	1.45	0.67	1.23	1.43	1.52	3.46	2.18	5.08	6.28	3.44	3.22	5.49	3.38	3.24	0.01
Total	100.20	99.28	99.92	99.00	98.63	99.25	99.73	99.39	98.51	100.10	100.50	99.35	98.51	100.10	100.10	
Trace Elements in ppm																
Sc	12	12	13	19	9	9	9	7	6	7	5	5	5	5	5	1
Be	< 1	< 1	< 1	< 1	1	< 1	< 1	1	< 1	< 1	1	1	1	1	1	1
V	130	125	123	183	84	84	88	75	89	94	68	66	63	63	65	5
Cr	50	50	50	60	40	40	40	30	20	20	20	< 20	20	20	20	20
Co	9	14	15	21	10	11	9	8	6	8	8	8	7	8	8	1
Ni	40	30	30	40	20	20	40	< 20	< 20	< 20	< 20	< 20	< 20	< 20	< 20	20
Cu	400	180	80	90	40	120	370	330	140	430	120	90	50	150	70	10
Zn	240	110	70	140	330	260	140	190	200	100	880	850	1410	210	200	30
Ga	19	19	18	20	18	18	17	17	20	18	19	20	18	19	19	1
Ge	1	< 1	1	1	1	1	1	1	1	1	1	1	< 1	< 1	< 1	1
As	13	16	< 5	< 5	9	10	8	46	24	29	35	17	81	52	84	5
Rb	3	24	28	8	9	18	8	8	14	15	14	9	26	23	52	2
Sr	493	508	493	578	469	448	475	407	547	637	617	636	344	556	522	2
Y	7	10	11	8	8	9	8	7	6	4	4	4	4	4	6	1
Zr	87	146	132	57	108	115	101	116	84	81	82	83	81	82	87	2
Nb	2	2	2	1	2	2	2	2	< 1	2	2	2	2	2	2	2
Mo	4	6	< 2	< 2	< 2	< 2	24	< 2	< 2	13	< 2	< 2	< 2	< 2	< 2	2
Ag	< 0.5	< 0.5	< 0.5	< 0.5	< 0.5	< 0.5	< 0.5	< 0.5	< 0.5	< 0.5	< 0.5	< 0.5	< 0.5	< 0.5	< 0.5	0.5
Sn	< 1	< 1	< 1	< 1	< 1	2	< 1	< 1	< 1	1	< 1	< 1	< 1	< 1	< 1	1
Sb	0.8	0.5	< 0.5	< 0.5	0.9	0.7	< 0.5	< 0.5	< 0.5	< 0.5	< 0.5	< 0.5	< 0.5	< 0.5	< 0.5	0.5
Cs	< 0.5	1.1	0.8	0.5	< 0.5	< 0.5	< 0.5	< 0.5	0.6	2.5	0.7	0.7	1.4	1.8	0.6	0.5
Ba	138	370	389	171	290	433	201	210	239	218	379	410	245	411	535	2
La	10.1	11.6	11.5	7.8	8.7	14.0	10.7	12.9	11.2	10.3	11.8	11.6	11.2	11.8	11.7	0.1
Ce	22.1	26.1	26.3	18.2	19.4	29.6	23.6	26.3	23.8	21.7	24.2	24.1	22.9	23.9	24	0.1
Pr	2.8	3.41	3.35	2.43	2.53	3.59	2.88	3.04	2.69	2.72	2.95	2.88	2.75	2.87	2.88	0.05
Nd	11.6	14.5	13.7	10.4	10.8	13.5	11.9	11.4	11.3	11.2	11.3	11.1	10.5	10.9	10.8	0.1
Sm	2.3	3.1	3.1	2.6	2.3	2.6	2.2	2.1	2.2	2.3	2.2	2.2	2.0	1.9	2.1	0.1
Eu	0.82	0.89	0.77	0.9	0.66	0.72	0.67	0.65	0.70	0.76	0.7	0.65	0.75	0.67	0.66	0.05
Gd	2	2.5	2.6	2.2	1.9	2.1	1.8	1.6	1.4	1.6	1.5	1.3	1.3	1.3	1.4	0.1
Tb	0.3	0.4	0.4	0.4	0.3	0.3	0.3	0.2	0.2	0.2	0.2	0.2	0.2	0.2	0.2	0.1
Dy	1.7	2.2	2.3	2.1	1.8	1.7	1.7	1.4	1.1	1.3	0.9	0.9	0.9	0.9	1	0.1
Ho	0.3	0.4	0.5	0.4	0.3	0.3	0.3	0.2	0.2	0.2	0.2	0.2	0.2	0.2	0.2	0.1
Er	0.9	1.2	1.3	1.1	0.9	0.9	0.9	0.7	0.5	0.6	0.4	0.4	0.4	0.4	0.5	0.1
Tm	0.13	0.18	0.19	0.16	0.13	0.13	0.12	0.1	0.07	0.08	0.06	0.06	0.06	0.06	0.06	0.05

13

Table 4 (*continued*)

Yb	0.8	1.1	1.2	1	0.8	0.8	0.8	0.7	0.4	0.5	0.4	0.4	0.4	0.4	0.4	0.1
Lu	0.13	0.17	0.18	0.16	0.13	0.13	0.12	0.11	0.07	0.08	0.07	0.06	0.06	0.06	0.06	0.01
Hf	2.1	3.3	2.9	1.4	2.7	2.8	2.4	2.7	2.1	1.8	1.8	2	1.9	1.9	2	0.2
Ta	0.2	0.1	0.2	0.1	0.2	0.2	0.2	0.2	0.2	0.1	0.1	0.2	0.1	0.1	0.2	0.1
W	2	2	1	3	3	5	5	2	2	3	5	4	2	3	3	1
Tl	< 0.1	0.2	0.2	< 0.1	0.1	0.1	0.1	0.1	0.1	0.2	0.1	0.1	0.3	0.3	0.5	0.1
Pb	24	11	8	9	185	49	17	22	20	19	35	57	38	19	29	5
Th	2.3	2.7	3	1.7	3.7	3.5	2.7	3.7	0.7	1.9	2.2	2.2	2.6	2.9	2.1	0.1
U	0.7	0.8	0.9	0.4	0.9	1	0.8	0.8	0.6	0.6	0.6	0.7	0.8	0.9	0.7	0.1

Notes:
- [1]Rock units. GRD: Granodiorite; TON: Tonalite; FRHP: Feldspar and Rounded Hornblende Porphyry; FHP: Feldspar and Hornblende Porphyry.
- [2]Abreviations. Bt: Biotite; Hbl: hornblende; DL: detection limit.
- [3]Chemical classification according to silica contents at anhydrous basis. BA: basaltic andesite; A: andesite; D: dacite; R: rhyolite.

Teniente (34°04′S) have also been considered (Fig. 1a). For both areas, this includes the analyses reported for (i) the regional Miocene background magmatism (Kay et al., 2005; Bergoeing, 2016), (ii) the pre-mineralization stocks (Stern et al., 2011; Bergoeing, 2016) and (iii) the *syn*-mineralization stocks (Reich et al., 2003; Stern et al., 2011; Bergoeing, 2016).

Analyzed samples from the Brahma prospect cover a continuous range in SiO_2 contents between ~ 61% and 70%, with the exception of one sample of the GRD with a value of 55% (Fig. 8a). According to the plutonic TAS diagram (not shown), the former samples correspond to diorites and granodiorites and the latter to a gabbrodiorite. In addition, differences in composition are observed between units respect to silica contents, with most samples of the GRD and FRHP showing lower contents of this parameter (~61–64%) than the TON and FHP (66–69%; Table 4). According to different criteria, the samples show a sub-alkaline character with calc-alkaline affinities (e.g. Fig. 8a, b). In Harker variation diagrams these display collinear patterns for many elements, in particular for major elements (e.g. Fig. 8a, c), but subtle differences emerge between the equigranular (GRD, TON) and the porphyritic (FHP, FRHP) units. While covering a similar silica content, the porphyritic units show for numerous elements a more enriched/evolved character, as seen for example in the lower contents of elements such as MgO (e.g. Fig. 8c), Sc, V, Cr and Co. Compared against the background magmatism from nearby localities, in whole the samples from the Brahma prospect display concordant patterns for the majority of the parameters previously discussed (e.g. Fig. 8) excepting for more marked calc-alkaline affinities (e.g. Fig. 8b).

In terms of REE (*rare earth elements*) composition of all studied samples show an enriched signature, ranging between 2 and 60 times the chondritic value, with a preferential enrichment of LREE (*light REE*) over HREE (*heavy REE*; Fig. 9a). Notoriously, in the chondrite normalized diagram the studied units configure two marked groups as it was previously noted for other geochemical parameters. This is seen in a more fractionated nature of the porphyritic units (FHP, FRHP) respect to the equigranular ones (GRD, TON), which results from lower HREE contents of the former at similar LREE contents of both groups (Fig. 9a). Within each group samples show fairly subparallel patterns and Eu anomalies are negligible (Fig. 9a). In N-MORB normalized multielement spider diagrams (Fig. 9b), studied samples show the typical characteristics of arc signatures, such as selective enrichment of LILE (*large ion lithophile elements*) over HFSE (*high field strength elements*) along with a marked Nb-Ta through. Compared against the background and local magmatism, two main observations for the parameters described can be highlighted for the units of the Brahma prospect: (i) their higher degree of fractionation which also results from mostly lower HREE contents (Fig. 9a) and (ii) their apparently less enriched nature as seen from the lower contents of numerous HFSE elements they display at similar silica contents (Th, Nb, Ta, Ce, P_2O_5, Zr, Hf, Sm, Y, Yb; Fig. 9b). In terms of Hf isotopic composition the studied units reveal juvenile signatures, with $\varepsilon_{Hf}(t)$ values between + 8.6 and + 11.2, and they also display a slight tendency towards lower values with decreasing age (Fig. 9d).

The studied units show several geochemical characteristics that indicate adakitic-like signatures, a feature widely recognized in intrusives related to mineralization in porphyry copper deposits (e.g. Kay and Mpodozis, 2001; Oyarzún et al., 2001; Reich et al., 2003; Kay et al., 2005; Stern et al., 2011; Perelló et al., 2012). This is seen in discriminating diagrams of La/Yb vs. Yb and Sr/Y vs. Y where most samples plot in the adakite-like rocks field (Fig. 9e, f). This signature is much more pronounced for the porphyritic units (FHP, FRHP) than for the equigranular ones (GRD, TON), in accordance to the different patterns both groups display in normalized REE diagrams (Fig. 9a). In addition, altogether the intrusive units of the Brahma prospect separate clearly from the background igneous units of the nearby localities and the whole pattern is analogous to what is seen in the mineralized areas of the Los Pelambres and El Teniente deposits (Fig. 9e, f). However, the studied samples from the Brahma prospect do not reach the extremely
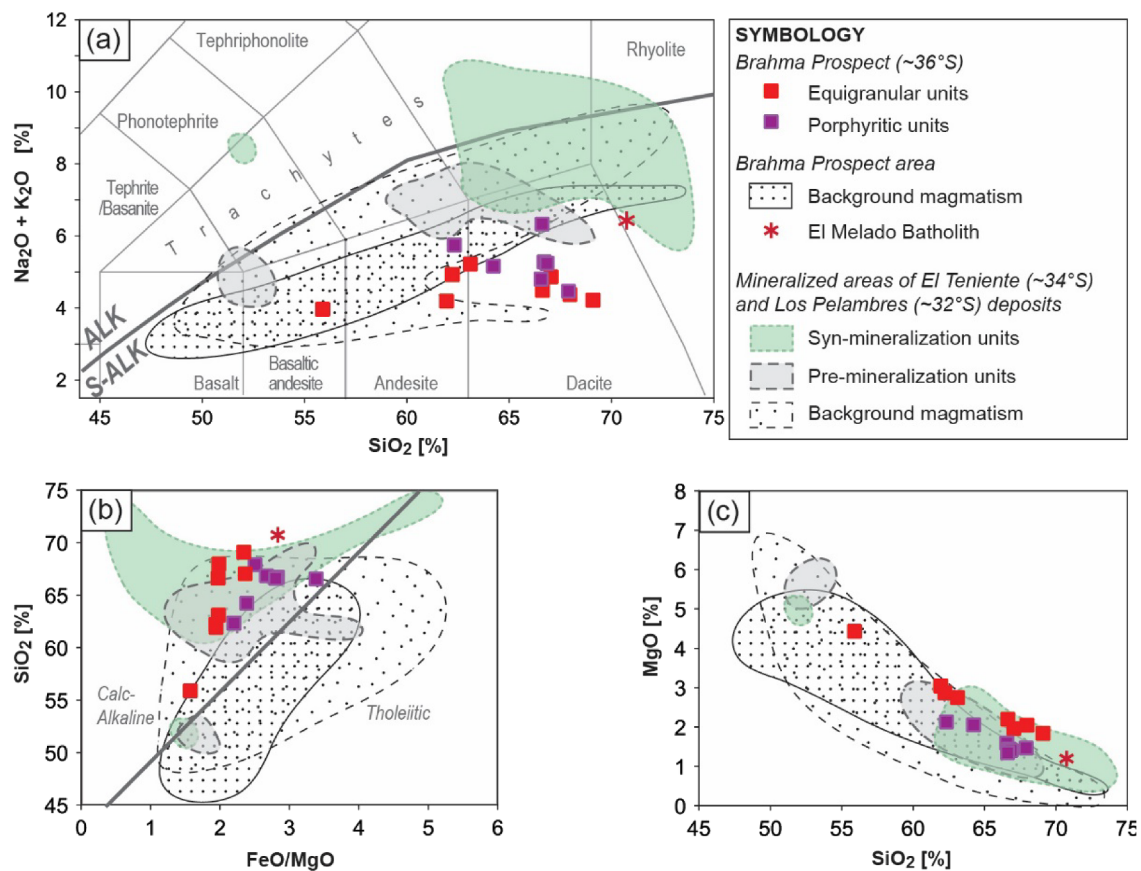
Fig. 8. Major element chemistry of the main intrusive units of the Brahma prospect. Diagrams correspond to: (a) TAS, (b) %SiO₂ vs. FeO/MgO, and (c) %MgO vs. % SiO₂. In (a) and (b) the magmatic series subdivisions are after Irvine and Baragar (1971) and Miyashiro (1974). In all diagrams the fields defined by other relevant magmatic units from Central Chile have been included for comparison. These correspond to the Miocene igneous units representing: (i) the background magmatism from the nearby areas of the Brahma prospect (~36°S; Vergara et al., 1999; Rojas del Castillo, 2018), and (ii) the background, pre-mineralization and *syn*-mineralization magmatism from the areas of El Teniente (~34°S; Kay et al., 2005; Stern et al., 2011) and Los Pelambres (~32°S; Reich et al., 2003; Bergoeing, 2016) deposits. Abbreviations correspond to ALK: alkaline; S-ALK: sub-alkaline.

high La/Yb and Sr/Y ratios documented for mineralized units from the latter two areas. Remarkable features are also observed comparatively in REE patterns displayed by all these units. The equigranular units from the Brahma prospect (GRD, TON) are similar to those of the pre-mineralization intrusives from the Los Pelambres and El Teniente deposits (Fig. 9c). In turn, patterns displayed by the porphyritic units (FHP, FRHP) are within the range of the *syn*-mineralization units from the latter areas (Fig. 9c).

5. Discussion

5.1. Main geological features of the Brahma prospect

The Brahma hydrothermal system covers an area of 6 km² and is open laterally and at depth (Burns et al., 2008; Fig. 2). Outcrops and drill cores from exploration boreholes show the presence of Cu, Mo, Zn and Pb mineralization hosted in intrusive porphyritic and equigranular rocks, and hydrothermal breccias. The feldspar-destructive alteration assemblages (sericitic and sericite-chlorite, as defined in Sillitoe, 2010, phyllic as defined in Corbett and Leach, 1998) are best developed within the study area and are superimposed onto an early and poorly mineralized potassic alteration. The mineralization is present as disseminations and stockwork veins, which are mostly related to feldspar-destructive alteration.

Of the 10 identified types of veins, early potassic types I and II (Fig. 5a,b and Fig. 6a; Table 1) can be correlated with EB and A type veins (respectively) as defined by Gustafson and Hunt (1975) and

Gustafson and Quiroga (1995) at the El Salvador porphyry Cu-Mo deposit. Type III veins (Fig. 5c; Table 1), corresponding to sericite-chlorite-quartz-pyrite alteration, correlates with C type veins (Gustafson and Quiroga 1995), while later veins associated with sericite-quartz ± clays, sericite-chlorite-quartz-pyrite and clays-iron oxides-sericite alterations (types IV, V, VI, VII, VIII and X; Fig. 5d-h and j; Table 1) could be correlated with D type veins (Gustafson and Hunt, 1975). Vein types IV and X also show characteristics of type E polymetallic veins defined by Lang et al. (2013) at the Pebble porphyry Cu-Mo-Au deposit (Alaska); whereas chlorite-epidote vein type IX (Fig. 5i; Table 1) could be associated to H vein type, defined in the same study.

Lithology, alteration and mineralization characteristics indicate that the Brahma prospect forms part of a porphyry Cu-Mo system with incipient and irregular development of Cu secondary enrichment that is hosted preferentially in zones of high permeability. According to the typical alteration and mineral zonation of this kind of deposits (Lowell and Guilbert, 1970; Sillitoe, 2010), the studied area seems to correspond to the upper portion of a porphyry copper system, in the pyrite shell described by Lowell and Guilbert (1970) and the Cu–Zn–Pb mineralization zone described by Sillitoe (2010) and Kouzmanov and Pokrovski (2012), the latter also agreeing with the predominance of late veins related to acidic alterations (phyllic ± argillic). In many Chilean Miocene-Pliocene porphyry Cu deposits the main copper mineralization is related with breccia bodies (Skewes and Stern, 1995; Serrano et al., 1998; Skewes et al., 2002; Maksaev et al., 2004), which in turn commonly show mineral zonation (Sillitoe, 2010). Considering this, the hypogene copper mineralization in the Brahma prospect could
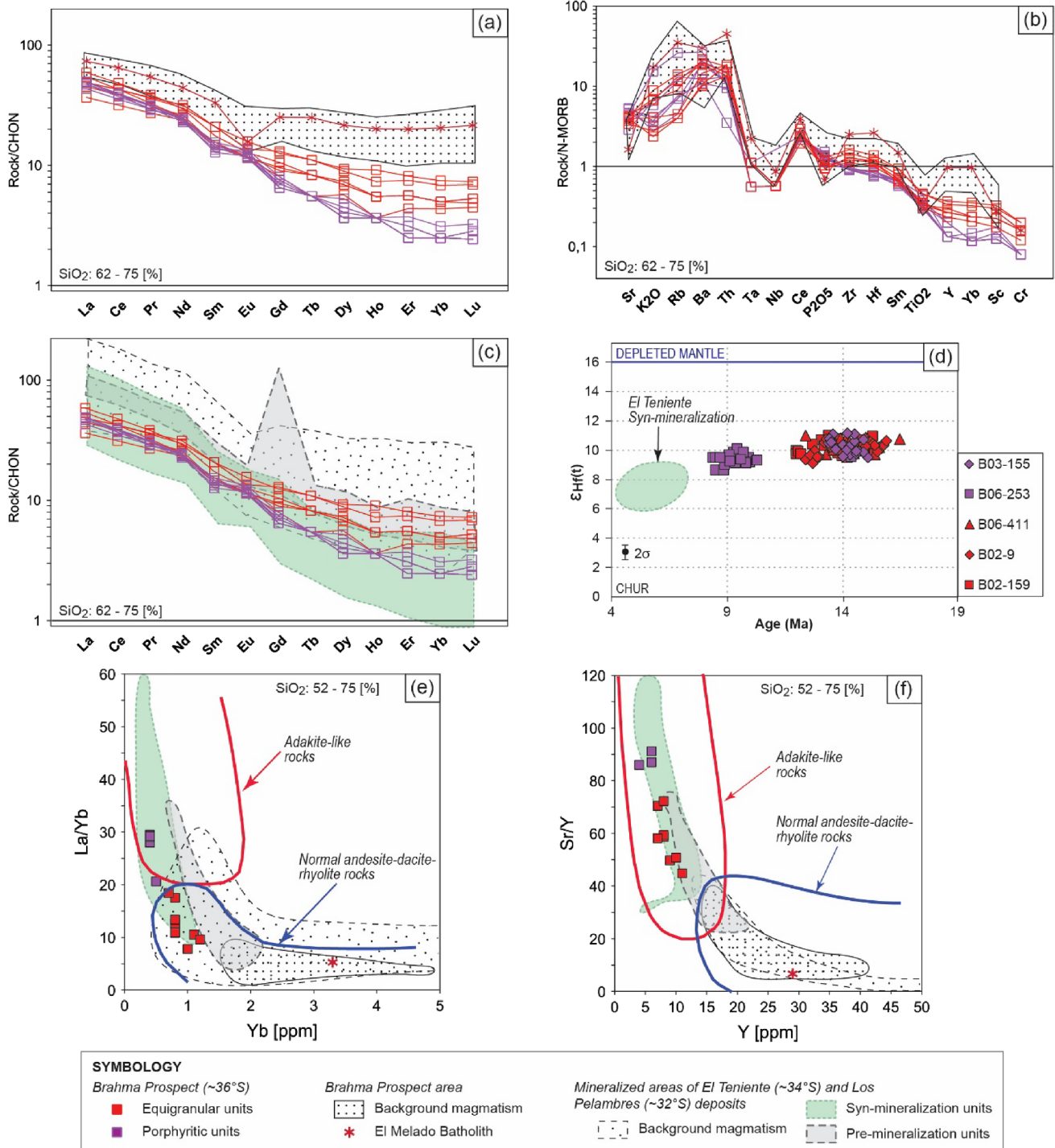
Fig. 9. General compositional features, in terms of trace element data, of the main intrusive units of the Brahma prospect. (a) Chondrite normalized REE diagram and (b) multi-element spidergram, both exclusively displaying data of the Brahma prospect region. (c) Chondrite normalized REE diagram including data from other relevant mineralized areas. (d) Hf isotopic composition. In the latter diagram, chondritic (CHUR; Blichert-Toft and Albarède, 1997) and depleted mantle reservoirs (Vervoort and Blichert-Toft, 1999) are shown for reference, and data from El Teniente deposit has been included for comparison (Muñoz et al., 2012). (e) and (f) display fertility diagrams of La/Yb vs. Yb and Sr/Y vs. Y, respectively. Fields for adakitic and normal andesite-dacite-rhyolite rocks after Richards and Kerrich (2007). Chondrite and N-MORB normalization respectively after McDonough and Sun (1995) and Pearce (1983). Displayed data for other relevant magmatic units from Central Chile as in Fig. 7.

be associated with breccias at depth, despite the fact that the mineralization observed in both breccia bodies is dominated by pyrite and sphalerite.

5.2. Temporal development of the deposit

Samples B06038-1 (vein type II) and B03111-5 (disseminated) record the oldest mineralization ages determined in the study area, which occurred at ∼ 14 Ma (Table 3), and such hydrothermal event is well correlated with the ages of its intrusive host units (GRD and FRHP;
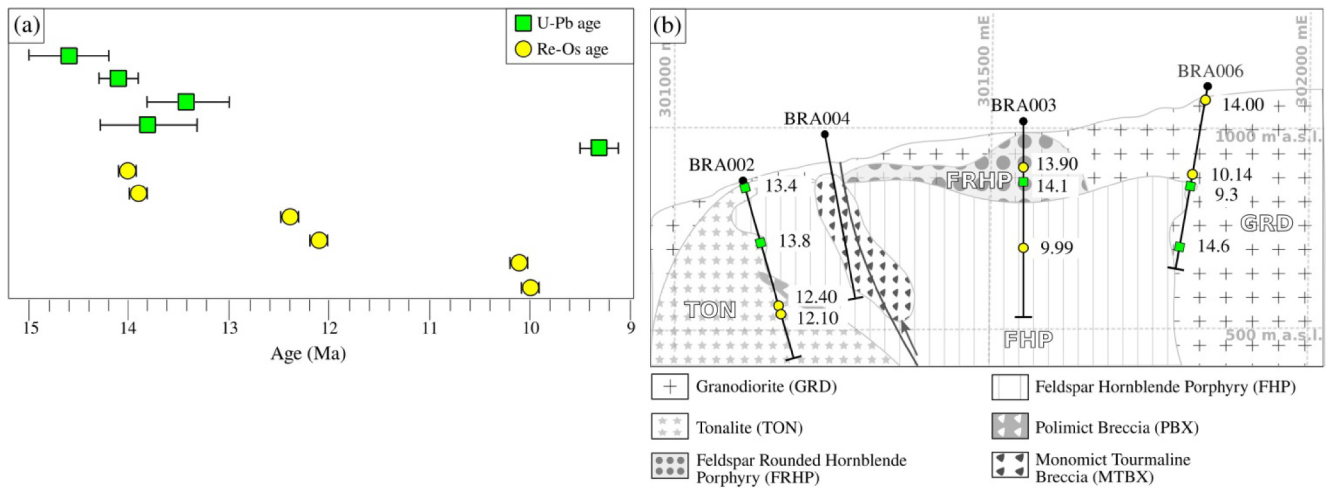
Fig. 10. (a) Summary of the primary and secondary mineral age determinations from the Brahma prospect in this study and (b) location of the corresponding samples. In (a) error bars are at 2σ level.

Fig. 10a). This indicates the presence of a ~ 14 Ma magmatic-hydrothermal event with associated early potassic and feldspar-destructive alteration assemblages, since the mineralization analyzed is related to such alteration types (Table 1). Molybdenite mineralization from type V veins (sericite–chlorite–quartz–pyrite alteration; samples B02315-7 and B02334-2; Table 3) represents a hydrothermal event of ~ 12 Ma. This is at least 1 m.y. younger than their intrusive host unit (TON; Fig. 10) and therefore it is unlikely that this molybdenite mineralization is correlated with this magmatic event. Molybdenite from type VII and IX veins (sericite–quartz ± clays feldspar-destructive and chlorite–epidote alteration respectively; samples B03310-2 and B06221-3; Table 3) show ages of ~ 10 Ma and corresponds to the youngest mineralization event recorded in the studied section. These results indicate that the poorly mineralized potassic alteration identified here is an event related to an early porphyry of ~ 14 Ma, probably the FRHP. Later feldspar-destructive alteration (phyllic ± argillic), which may represent a roof over a deeper mineralized potassic core, is related to younger porphyritic units, probably the FHP of 9.3 Ma.

Overall, the obtained ages correlate well with the cross-cutting relationships observed in the veins, where early potassic veins show the older ages and feldspar-destructive veins show younger ages. On the other hand, the cross-cutting relationships and the 10.14 Ma age obtained from the chlorite–epidote vein (type IX) confirms that this alteration is coeval with the sericite–quartz ± clays alteration and thus this would not be related to an early stage of the system. This suggests that chlorite–epidote alteration documented in the Brahma prospect could be related to a distal propylitic alteration from other nearby porphyry systems (e.g. from the Roblería and/or Calabozos porphyry copper targets documented by Sanchez and Motta, 2013; Fig. 1b).

An apparent age misfit is observed in a vein type VII sample showing a mineralization age about 0.7 to 0.5 m.y. older than its host rock, the FHP dated in 9.3 ± 0.2 Ma. It must be noted that radiometric determinations for such mineralization and intrusive events were made in samples separated from each other by approximately 430 m (Fig. 10b), therefore allowing the possibility that the mentioned host rock would correspond to a different and older porphyritic unit. However, petrographic and geochemical evidence strongly indicate that this corresponds to the FHP. Moreover, 6 of the 23 analyzed zircons of the dated FHP sample gave ages of about 10 Ma (Fig. 7), which suggests a crystallization age range wider than the sole central age determined for this unit. Whichever the case, it must be noted that the PBX body is composed, among other things, by FHP fragments (Fig. 3f, g) and thus the average age of the FHP unit constitutes a maximum age for this breccia unit and its associated mineralization (veins type X). The latter

suggest that the main mineralization event in the Brahma prospect is most likely related to hydrothermal fluids exsolved from the FHP intrusion and the PBX event. This mineralization event occurred at ~ 10 Ma and it would have extended after 9.3 Ma which is the age of the younger mineralized porphyry in the prospect (FHP).

In summary, the results obtained from the Re-Os age determinations indicate that there are at least three mineralization events within the prospect. These occurred at ~ 14, ~12 and ~ 10 Ma correlating well with the magmatic pulses of ~ 14 and ~ 9 Ma (Fig. 10). These results indicate that the Brahma prospect formed by at minimum of three magmatic-hydrothermal events and that the system was active for at least 4 to 5 m.y.

5.3. Igneous petrogenetic processes

The main intrusive units of the Brahma prospect show overall geochemical characteristics that are similar to those of the hosting volcano-plutonic Miocene Andean arc of the region (Vergara et al., 1999). This includes a juvenile character, as suggested by the Hf isotopic composition. However, a marked difference is their comparatively more evolved and fractionated nature which argues for a particular scenario for their formation. On one hand, the juvenile signatures shown by both groups suggest similar geochemical components involved in their magma genetic processes, in particular a compositionally similar source and/or low degree of crustal contamination. On the other hand, the markedly more evolved and fractionated character of the Brahma prospect units argues for extensive magmatic chamber processes as also supported by the intense, almost continuous, and long-lived record of magmatic activity in that area. At the prospect scale, the compositional and mineralogical characteristics indicate that all the intrusive units share a similar petrogenetic evolution dominated by the crystallization of plagioclase, quartz, amphibole and subordinated alkali feldspar and biotite. In particular, an important involvement of amphibole, as a fractionating assemblage and/or in the magmatic source, could explain the lower contents of MREE (*middle REE*) and HREE respect to the local background magmatism (Fig. 9a). This characteristic is also partly responsible for their adakite-like signature (Fig. 9e, f), similarly to numerous intrusive units related to porphyry copper mineralization for which the role of amphibole in magma genesis has been pointed as a likely cause (e.g. Richards and Kerrich, 2007). In addition, such signature is in particular similar to that displayed by the mineralization related intrusives of the El Teniente and Los Pelambres deposits, two highly endowed Andean copper deposits of Cenozoic age located further north. It must also be noted that, despite

other geochemical and isotopic similarities, the porphyritic units of the Brahma prospect show a more marked adakite-like signature and a more evolved nature than the equigranular units. This feature supports the existence of a complex deep feeding magmatic reservoir which should be at least compositionally zoned in order to allow the coexistence of the different igneous units observed.

5.4. The Brahma prospect in the context of Andean metallogenesis

The porphyry Cu deposits of Central Chile belong to one of the most enriched Cu provinces in the world, with > 180 Mt of copper (resources plus production; Camus, 2003; Cannell et al., 2005) identified in five Miocene to Pliocene deposits (Fig. 1a). These deposits share many characteristics like being related to porphyritic intrusions hosted in volcano-sedimentary rocks, magmatic-hydrothermal activity associated to main regional structures, copper mineralization hosted in breccia bodies, among others (e.g. Camus, 2003; Maksaev et al., 2007). From a geochronological point of view, one of the most remarkable features of these porphyry Cu deposits, and of other giant porphyry deposits in the world, is their genetic relation to long term and multiple episodes of magmatism and mineralization (e.g Butte, Montana, USA, Brimhall, 1979; El Salvador, Chile, Cornejo et al., 1997; Chuquicamata, Chile, Reynolds et al., 1998; Bagdad, Arizona, USA, Barra et al., 2003; El Teniente, Chile, Maksaev et al., 2004). These *syn*-mineralization intrusive units usually show a spatial relation with precursor large polyphasic plutonic bodies such as Las Gualtatas Pluton near Los Pelambres (21.6–18.4 Ma; Bertens et al., 2006), Río Blanco Pluton and San Francisco Batholith in the area of Río Blanco-Los Bronces (14.7–8.2 Ma; Deckart et al., 2005; Deckart et al., 2010) and El Teniente plutonic complex (12–7 Ma; Kurtz et al., 1997; Maksaev et al., 2004; Cannell et al., 2005). The results of our study evidence that all the mentioned characteristics are observed in the Brahma prospect: this represents a hydrothermal system that has been fed almost continuously by magmatism from at least 14 Ma until 9 Ma and which seems to be related with the older El Melado Batholith (Fig. 1b; 23.8–14.2 Ma; Drake et al., 1982; Nelson et al., 1999; Spikings et al., 2008; Cabezas et al., 2018). The intrusive and mineralization/alteration ages determined for Brahma prospect are similar to those reported for the Los Pelambres deposit, where the magmatic activity started at ~ 13.9 Ma and the main mineralization event developed at ~ 11 Ma (Fig. 11; Bertens et al., 2003, 2006; Perelló et al., 2012).

Another significant feature of the Miocene-Pliocene Cu deposits of Central Chile is the presence of regional NW and NE striking structures

Fig. 11. Geochronology summary of the main porphyry Cu-Mo deposits from the Miocene-Pliocene metallogenic belt in Central Chile. The Brahma prospect shows similar ages to the Los Pelambres-El Pachón deposit. The mineralization age in the Brahma prospect has not been completely constrained, as indicated by the question marks, due to the interpreted presence of a potential younger mineralized porphyry unit. Geochronological data taken from Bertens et al (2003, 2006), Maksaev et al. (2004), Deckart et al. (2005, 2013, 2014), Muñoz (2008) and Perelló et al. (2012). Abbreviations correspond to LP: Los Pelambres; EP: El Pachón; RB: Río Blanco; LB: Los Bronces.

that apparently control mineralization and the emplacement of the porphyritic stocks and breccia bodies (Camus, 2003; Cannell et al., 2005; Maksaev et al., 2007; Piquer et al., 2015). These structures likely represent ancient normal faults that controlled second order tectonic compartments of the Abanico basin and which were reactivated as reverse faults during Mio-Pliocene east–west contraction (Camus, 2003; Piquer et al., 2015). For the Brahma prospect area there are no structural studies of regional scale to asses such observation. However, local studies at the deposit scale and its surroundings show that, like other Mio-Pliocene deposits in Chile, this is also controlled by a series of NW striking structures and a major NS to NE striking fault (Fig. 2a) (Burns et al., 2008).

Compositional characteristics of the igneous units correspond to another feature in common between the Brahma prospect and the Mio-Pliocene porphyry copper deposits of Central Chile (Figs. 8, 9). In particular, the intrusions have high La/Yb and Sr/Y ratios that correspond with an adakite-like signature commonly recorded in porphyry Cu related intrusions worldwide (e.g. Baldwin and Pearce, 1982; Kay and Mpodozis, 2001; Oyarzún et al., 2001; Cooke et al., 2005; Lopez, 2010; Sun et al., 2011; Stern et al., 2011; Chiaradia, 2014). The origin of such geochemical signature in mineralization related magmas is still a matter of debate and has been variably attributed mainly to two processes. On one hand, this has been invoked to result from magma genesis under a crustal thickening scenario, where there is an increasing involvement of high pressure minerals in the residual and/or crystallizing assemblages (e.g. Kay and Mpodozis, 2001). Alternatively, the adakite-like signature in mineralization related magmas would result from extensive magma chamber fractionation of particular mineral assemblages (e.g. Richards and Kerrich, 2007; Stern et al., 2011). The first of these hypotheses is in part restricted for the Brahma case. The prospect currently sits in an Andean area overlying a 40 km thick crust (e.g. Tassara et al., 2006; Tassara and Echaurren, 2012), thus it never reached sufficient thickness for garnet formation in the mineral assemblages at the crustal basal level. Interestingly, a similar scenario has been inferred in the case of the Los Pelambres deposit (e.g Kay and Mpodozis, 2001; Reich et al., 2003). The second hypothesis could be more appropriate given the relation of the Brahma prospect to a long-lived and complex magmatic reservoir previously inferred.

Finally, it is also important to note that although the mean grades of Cu and Mo from drill core samples are sub-economic, mineralization in the Brahma prospect confirms the presence of Cu and Mo within the hydrothermal system. The above in addition with the multiplicity and long-life of the magmatic hydrothermal events would indicate favorable conditions to generate an economic porphyry Cu-Mo deposit. As a result, the Brahma porphyry copper prospect shows an interesting exploration potential, which at present has only been drilled to the upper parts of the system, the prospect remaining sub explored at present.

6. Summary and conclusions

(1) The Brahma prospect corresponds to a porphyry type deposit in which mineralization is hosted in and is related to intrusive rocks. The main intrusive units that comprise it correspond to: Granodiorite (GRD), Feldspar and Rounded Hornblende Porphyry (FRHP), Tonalite (TON) and Feldspar and Hornblende Porphyry (FHP). In addition, related to the emplacement of the latter intrusives there are numerous *syn*-mineralization igneous and hydrothermal breccias that are mostly polymict with rock flour and tourmaline cement. The dominant alteration present corresponds to a feldspar-destructive alteration (phyllic ± argillic) that is highly pervasive in the most permeable zones and which overprints an earlier weak and poorly mineralized potassic alteration. The mineralization corresponds to pyrite and less chalcopyrite, molybdenite, sphalerite and chalcocite, which occur mainly as disseminations and veins. According to the classic models that characterize these kind of deposits (Lowell and Guilbert, 1970; Sillitoe, 2010), the studied area seems to correspond to the proximal
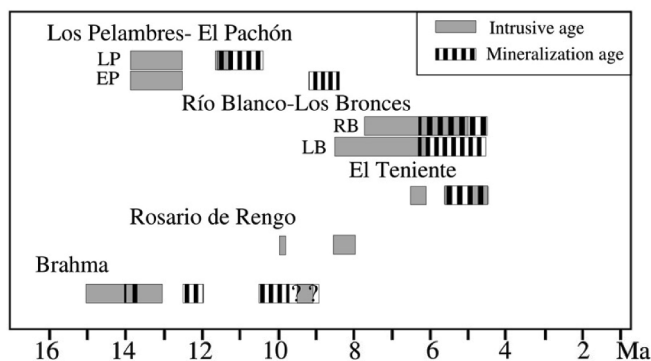
upper portion of a porphyry system, where the main phyllic/argillic alteration zones predominant in the district, represent a larger and younger expression of a potential deeper system, which overprints the earlier weak potassic development.

(2) Primary mineral age determinations indicate at least three magmatic events occurred at ~ 17 Ma, ~14 Ma and ~ 9 Ma. The intrusion of the units GRD, FRHP and TON occurred almost simultaneously at ~ 14 Ma and were followed by the intrusion of the FHP at ~ 9 Ma. Alteration-mineralization age determinations reveal an early mineralization stage coeval with the magmatic event of ~ 14 Ma. An intermediate mineralization stage of ~ 12 Ma was identified suggesting the presence of another intrusive unit not recognized in this study. Finally, the last and major mineralization event recorded show ages of around 10 Ma, however, according to the presence of a younger mineralized porphyritic unit (FHP; 9.3 Ma) and a strongly mineralized polymict breccia (PBX) with clasts of the latter unit, this event should have extended from ~ 10 Ma to after 9.3 Ma (Fig. 11).

(3) Geochemical characteristics indicate that intrusive units from the Brahma prospect formed from arc magmatism that developed on the continental margin during middle to late Miocene. The prospect is hosted in the primitive volcanic rock series of the Colbún Formation (Vergara et al., 1999) and its intrusive units also show juvenile signatures. This indicates that mineralization related magmas share with the background magmatism a similar genesis in terms of the source and/or the involvement of low degrees of crustal contamination. However, they are markedly more evolved and fractionated regardless of the minor geochemical variations they record. These characteristics along with the long-term record of magmatic activity strongly support the existence of a long-lived and complex deep feeding magmatic reservoir.

(4) The Brahma prospect shows geological characteristics similar to other Miocene-Pliocene porphyry Cu deposits in Central Chile such as Los Pelambres and, to a lesser extent, El Teniente deposits. Moreover, its Miocene age agrees with the age reported for other porphyry copper targets/deposits occurring along the western slope of the Andes south of the El Teniente deposit (34°05′S; Rosario de Rengo at 34°31′S, 9.89 – 8.43 Ma, Muñoz, 2008; Infiernillo, 35°09′S, 8.29 ± 0.02 Ma, Vale-Exploraciones, 2017). Altogether, this suggests the continuation of the Miocene-Pliocene metallogenic belt southerly from the El Teniente deposit (34°05′S) to at least the location of the Brahma prospect (35°45′S).

Declaration of Competing Interest

The authors declare that they have no known competing financial interests or personal relationships that could have appeared to influence the work reported in this paper.

Acknowledgments

Appendix A. Supplementary data

Supplementary data to this article can be found online at https://

doi.org/10.1016/j.oregeorev.2020.103522.

References

Astaburuaga, D., 2014. Evolución estructural del límite Mesozoico-Cenozoico de la Cordillera Principal entre 35°30′ y 36°S, Región del Maule, Chile, M. Sc. Thesis, Departamento de Geología, Universidad de Chile, Santiago, p. 128.

Baldwin, J.A., Pearce, J.A., 1982. Discrimination of productive and nonproductive porphyritic intrusions in the Chilean Andes. Econ. Geol. 77, 664–674.

Barra, F., Ruiz, J., Mathur, R., Titley, S., 2003. A Re–Os study of sulfide minerals from the Bagdad porphyry Cu–Mo deposit, northern Arizona, USA. Miner. Deposita 38, 585–596.

Bergoeing, J.P., 2016. Evolución geoquímica del magmatismo de la región de Los Pelambres (31°S) entre el Cretácico Superior y el Mioceno Superior: Implicancias para la evolución tectónica y metalogénica de los Andes de Chile Central, Undergraduated Thesis, Departamento de Geología, Universidad de Chile, p. 111.

Bertens, A., Clark, A., Barra, F., Deckart, K., 2006. Evolution of the Los Pelambres-El Pachón porphyry copper-molybdenum district, Chile/Argentina, in: XI Congreso Geológico Chileno, Antofagasta, pp. 179-181.

Bertens, A., Deckart, K., Gonzalez, A., 2003. Geocronología U-Pb, Re-Os y 40Ar/39Ar del pórfido Cu-Mo Los Pelambres, Chile central, in: X Congreso Geológico Chileno, Concepción, (CD-ROM): 5.

Birck, J.L., Barman, M.R., Capmas, F., 1997. Re-Os Isotopic Measurements at the Femtomole Level in Natural Samples. Geostandards newsletter 21, 19–27.

Brimhall, G.H., 1979. Lithologic determination of mass transfer mechanisms of multiple-stage porphyry copper mineralization at Butte, Montana; vein formation by hypogene leaching and enrichment of potassium-silicate protore. Econ. Geol. 74, 556–589.

Burns, P., Marquez, E., Arias, S., 2008. Brahma Cu-Mo Porphyry, Chile: Unpublished report. Condor Resources Incorporated, p. 452.

Cabezas, L.M., Muñoz, M., Rojas del Castillo, M., 2018. Nuevos antecedentes estratigráficos y dataciones radiométricas U-Pb en el valle superior del río Maule a los ~35°50′S, Chile Central: Implicaciones en la evolución geológica Cenozoica, in: XV Congreso Geológico Chileno, Concepción, pp. 1099-1102.

Cahill, T., Isacks, B.L., 1992. Seismicity and shape of the subducted Nazca plate. J. Geophys. Res. Solid Earth 97, 17503–17529.

Camus, F., 2003. Geología de los Sistemas Porfíricos en los Andes de Chile., Servicio Nacional de Geología y Minería, Santiago, Chile, p. 267.

Cannell, J., Cooke, D.R., Walshe, J.L., Stein, H., 2005. Geology, mineralization, alteration, and structural evolution of the El Teniente porphyry Cu-Mo deposit. Econ. Geol. 100, 979–1003.

Cooke, D.R., Hollings, P., Walshe, J.L., 2005. Giant porphyry deposits: characteristics, distribution, and tectonic controls. Econ. Geol. 100, 801–818.

Corbett, G.J., Leach, T.M., 1998. Southwest Pacific Rim gold-copper systems: structure, alteration, and mineralization. Society of Economic Geologists.

Cornejo, P., Tosdal, R.M., Mpodozis, C., Tomlinson, A.J., Rivera, O., Fanning, C.M., 1997. El Salvador, Chile porphyry copper deposit revisited: Geologic and geochronological framework. Int. Geol. Rev. 39, 22–54.

Creaser, R.A., Papanastassiou, D.A., Wasserburg, G.J., 1991. Negative thermal ion mass spectrometry of osmium, rhenium and iridium. Geochim. Cosmochim. Acta 55, 397–401.

Culbert, R., 2007. Technical report on the Brahma copper property of south-central Chile: Unpublished report. Condor Resources incorporated, p. 14.

Charrier, R., Baeza, O., Elgueta, S., Flynn, J.J., Gans, P., Kay, S.M., Muñoz, N., Wyss, A.R., Zurita, E., 2002. Evidence for Cenozoic extensional basin development and tectonic inversion south of the flat-slab segment, southern Central Andes, Chile (33–36°S.L.). J. S. Am. Earth Sci. 15, 117–139.

Charrier, R., Pinto, L., Rodríguez, M.P., 2007. Tectonostratigraphic evolution of the Andean Orogen in Chile. In: Moreno, T., Gibbons, W. (Eds.), The Geology of Chile. The Geological Society, London, pp. 21–114.

Charrier, R., Ramos, V.A., Tapia, F., Sagripanti, L., 2015. Tectono-stratigraphic evolution of the Andean Orogen between 31° and 37°S (Chile and Western Argentina). Geological Society, London, Special Publications 399, 13–61.

Chiaradia, M., 2014. Copper enrichment in arc magmas controlled by overriding plate thickness. Nat. Geosci. 7, 43.

Deckart, K., Clark, A., Cuadra, P., Fanning, M., 2013. Refinement of the time-space evolution of the giant Mio-Pliocene Río Blanco-Los Bronces porphyry Cu-Mo cluster, Central Chile: new U-Pb (SHRIMP II) and Re-Os geochronology and ⁴⁰Ar/³⁹Ar thermochronology data. Miner. Deposita 48, 57–79.

Deckart, K., Clark, A.H., Celso, A.A., Ricardo, V.R., Bertens, A.N., Mortensen, J.K., Fanning, M., 2005. Magmatic and hydrothermal chronology of the giant Río Blanco porphyry copper deposit, central Chile: Implications of an integrated U-Pb and ⁴⁰Ar/³⁹Ar database. Econ. Geol. 100, 905–934.

Deckart, K., Godoy, E., Bertens, A., Jerez, D., Saeed, A., 2010. Barren Miocene granitoids in the Central Andean metallogenic belt, Chile: Geochemistry and Nd-Hf and U-Pb isotope systematics. Andean. Geology 37.

Deckart, K., Silva, W., Spröhnle, C., Vela, I., 2014. Timing and duration of hydrothermal activity at the Los Bronces porphyry cluster: An update. Miner. Deposita 49, 535–546.

Drake, R.E., 1976. Chronology of cenozoic igneous and tectonic events in the central Chilean Andes — latitudes 35° 30′ to 36°S. J Volcanol. Geothermal Res. 1 (3), 265–284.

Drake, R.E., Charrier, R., Thiele, R., Munizaga, F., Padilla, H., Vergara, M., 1982. Distribución y edades K-Ar de volcanitas post-Neocomianas en la Cordillera Principal entre 32° y 36° LS, Implicaciones estratigráficas y tectónicas para el Meso-Cenozoico de Chile Central, in: III Congreso Geológico Chileno Concepción, 42–78.

Farías, M., Comte, D., Charrier, R., Martinod, J., David, C., Tassara, A., Tapia, F., Fock, A.,

2010. Crustal-scale structural architecture in central Chile based on seismicity and surface geology: Implications for Andean mountain building. Tectonics 29.

Frei, R., Nägler, T.F., Schönberg, R., Kramers, J.D., 1998. Re-Os, Sm-Nd, U-Pb, and stepwise lead leaching isotope systematics in shear-zone hosted gold mineralization: Genetic tracing and age constraints of crustal hydrothermal activity. Geochim. Cosmochim. Acta 62, 1925–1936.

Freydier, C., Ruiz, J., Chesley, J., McCandless, T., Munizaga, F., 1997. Re-Os isotope systematics of sulfides from felsic igneous rocks: Application to base metal porphyry mineralization in Chile. Geology 25, 775–778.

Giambiagi, L.B., Ramos, V.A., 2002. Structural evolution of the Andes in a transitional zone between flat and normal subduction (33° 30′–33° 45′ S), Argentina and Chile. J. S. Am. Earth Sci. 15, 101–116.

González, O., Vergara, M., 1962. Reconocimiento Geológico de la cordillera de los Andes entre los paralelos 35 y 38 latitud sur. Instituto de Geología, Universidad de Chile, Santiago, pp. 121.

Gustafson, L.B., Hunt, J.P., 1975. The porphyry copper deposit at El Salvador, Chile. Econ. Geol. 70, 857–912.

Gustafson, L.B., Quiroga, J., 1995. Patterns of mineralization and alteration below the porphyry copper orebody at El Salvador, Chile. Econ. Geol. 90, 2–16.

Karzulovic, J., Hauser, A., Vergara, M., 1972. Edades K/Ar en rocas volcánicas e intrusivas del área de los proyectos hidroeléctricos Colbún-Machicura-Melado, Empresa Nacional de electricidad, SA, VII Región, in: II Congreso Geológico Chileno, Arica, pp. J127-J135.

Irvine, T.N., Baragar, W.R.A., 1971. A Guide to the Chemical Classification of the Common Volcanic Rocks. Canadian J. Earth Sci. 8 (5), 523–548.

Kay, S.M., Godoy, E., Kurtz, A., 2005. Episodic arc migration, crustal thickening, subduction erosion, and magmatism in the south-central Andes. Geol. Soc. Am. Bull. 117, 67–88.

Kay, S.M., Mpodozis, C., 2001. Central Andes ore deposits linked to evolving shallow subduction systems and thickening crust. GSA Today 11, 4–9.

Kouzmanov, K., Pokrovski, G.S., 2012. Hydrothermal controls on metal distribution in porphyry Cu (-Mo-Au) systems. Society of Economic Geologists, Special Publication 16, 573–618.

Kurtz, A.C., Kay, S.M., Charrier, R., Farrar, E., 1997. Geochronology of Miocene plutons and exhumation history of the El Teniente region, Central Chile (34–35 8). Andean Geol. 24, 75–90.

Lang, J.R., Gregory, M.J., Rebagliati, C.M., Payne, J.G., Oliver, J.L., Roberts, K., 2013. Geology and magmatic-hydrothermal evolution of the giant Pebble porphyry copper-gold-molybdenum deposit, southwest Alaska. Econ. Geol. 108, 437–462.

Lopez, L., 2010. Características geoquímicas de rocas ígneas asociadas con pórfidos cupríferos chilenos. Andean Geol. 17, 3–19.

Lowell, J.D., Guilbert, J.M., 1970. Lateral and vertical alteration-mineralization zoning in porphyry ore deposits. Econ. Geol. 65, 373–408.

Ludwig, K.R., 2008. Isoplot 3.70, a Geochronological Toolkit for Microsoft Excel. Berkeley Geochronology Center Special Publication, 4, p. 77.

Maksaev, V., Munizaga, F., McWilliams, M., Fanning, C.M., Mathur, R., Ruiz, J., Zentilli, M., 2004. New chronology for El Teniente, Chilean Andes, from U-Pb, 40Ar/39Ar, Re-Os, and fission-track dating: implications for the evolution of a supergiant porphyry Cu-Mo deposit, in: Sillitoe, R.H., Perelló, J., Vidal, A. (Eds.), Andean Metallogeny: New Discoveries, Concepts and Updates. Society of Economic Geologists Special Publication, 11, pp. 15-54.

Maksaev, V., Townley, B., Palacios, C., Camus, F., 2007. Metallic ore deposits. In: Moreno, T., Gibbons, W. (Eds.), The Geology of Chile. The Geological Society, London, pp. 180–199.

Mathur, R., Ruiz, J., Munizaga, F., 2000. Relationship between copper tonnage of Chilean base-metal porphyry deposits and Os isotope ratios. Geology 28, 555–558.

Mathur, R., Ruiz, J., Tornos, F., 1999. Age and sources of the ore at Tharsis and Rio Tinto, Iberian pyrite belt, from Re-Os isotopes. Miner. Deposita 34, 790–793.

Muñoz, P., 2008. Antecedentes petrográficos, geoquímicos y geocronológicos de rocas intrusivas del sector Rosario de Rengo, Región del Libertador Bernardo Ó higgins., Undergraduated Thesis, Departamento de Geología, Universidad de Chile, Santiago, p. 109.

McDonough, W.F., Sun, S.S., 1995. The composition of the Earth. Chem. Geol. 120 (3–4), 223–253.

Miyashiro, A., 1974. Volcanic rock series in island arcs and active continental margins. Am. J. Sci. 274 (4), 321–355.

Muñoz, M., Charrier, R., Fanning, C.M., Maksaev, V., Deckart, K., 2012. Zircon trace element and O-Hf isotope analyses of mineralized intrusions from El Teniente ore deposit, Chilean Andes: constraints on the source and magmatic evolution of porphyry Cu-Mo related magmas. J. Petrol. 53 (6), 1091–1122.

Nelson, S.T., Davidson, J.P., Heizler, M.T., Kowallis, B.J., 1999. Tertiary tectonic history of the southern Andes: The subvolcanic sequence to the Tatara-San Pedro volcanic complex, lat 36°S. Geol. Soc. Am. Bull. 111, 1387–1404.

Oyarzún, R., Márquez, A., Lillo, J., López, I., Rivera, S., 2001. Giant versus small porphyry copper deposits of Cenozoic age in northern Chile: adakitic versus normal calc-alkaline magmatism. Miner. Deposita 36, 794–798.

Pardo, M., Comte, D., Monfret, T., 2002. Seismotectonic and stress distribution in the central Chile subduction zone. J. S. Am. Earth Sci. 15, 11–22.

Paton, C., Woodhead, J., Hellstrom, J., Hergt, J., Greig, A., Maas, R., 2010. Improved laser ablation U-Pb zircon geochronology through robust downhole fractionation correction. Geochem. Geophys. Geosyst. 11, Q0AA06.

Perelló, J., Sillitoe, R.H., Mpodozis, C., Brockway, H., Posso, H., 2012. Geologic setting and evolution of the porphyry copper-molybdenum and copper-gold deposits at Los Pelambres, Central Chile, in: Hedenquist, J.W., Harris, M., Camus, F. (Eds.), Geology and genesis of major copper deposits and districts of the world: A tribute to Richard H. Sillitoe. Society of Economic Geologist Special Publication, 16, pp. 79-104.

Pearce, J.A., 1983. Role of the sub-continental lithosphere in magma genesis at active continental margins. In: Hawkesworth, C.J., Norry, M.J. (Eds.), Continental basalts and mantle xenoliths. Shiva Publications, Nantwich, Cheshire, pp. 230–249.

Petrus, J., Kamber, B., 2012. VizualAge: a novel approach to laser Ablation ICP-MS U-Pb geochronology data reduction. Geostand. Geoanal. Res. 36, 247–270.

Piquer, J., Skarmeta, J., Cooke, D.R., 2015. Structural evolution of the Rio Blanco-Los Bronces District, Andes of Central Chile: controls on stratigraphy, magmatism, and mineralization. Econ. Geol. 110, 1995–2023.

Reich, M., Parada, M.A., Palacios, C., Dietrich, A., Schultz, F., Lehmann, B., 2003. Adakite-like signature of late Miocene intrusions at the Los Pelambres giant porphyry copper deposit in the Andes of Central Chile: metallogenic implications. Miner. Deposita 38, 876–885.

Reynolds, P., Ravenhurst, C., Zentilli, M., Lindsay, D., 1998. High-precision ${}^{40}Ar/{}^{39}Ar$ dating of two consecutive hydrothermal events in the Chuquicamata porphyry copper system, Chile. Chem. Geol. 148, 45–60.

Richards, J.P., 2003. Tectono-magmatic precursors for porphyry Cu-(Mo-Au) deposit formation. Econ. Geol. Bull. Soc. Econ. Geol. 98, 1515–1533.

Richards, J.P., 2005. Cumulative factors in the generation of giant calc-alkaline porphyry Cu deposits. Super porphyry copper and gold deposits: A global perspective 1, 7-25.

Richards, J.P., Kerrich, R., 2007. Special paper: adakite-like rocks: their diverse origins and questionable role in metallogenesis. Econ. Geol. 102, 537–576.

Rojas del Castillo, M., 2018. Petrogénesis ígnea de las rocas miocenas del curso alto del valle del río Maule y el valle del río Melado (35°45'S), Cordillera Principal, Región del Maule, Chile, Undergraduated Thesis, Departamento de Geología, Universidad Andrés Bello, Santiago, p. 110.

Ruiz, J., Mathur, R., 1999. Metallogenesis in continental margins: Re-Os evidence from porphyry copper deposits in Chile. Econ. Geol. 12, 59–72.

Sanchez, J., Motta, H., 2013. Proyecto Brahma-Austral; Campaña de exploración de los targets Teatino-Calabozo-Roblería: Unpublished report. Geovectra, p. 40.

Selby, D., Creaser, R.A., 2004. Macroscale NTIMS and microscale LA-MC-ICP-MS Re-Os isotopic analysis of molybdenite: Testing spatial restrictions for reliable Re-Os age determinations, and implications for the decoupling of Re and Os within molybdenite. Geochim. Cosmochim. Acta 68, 3897–3908.

Sernageomin, 2003. Mapa geológico de Chile: versión digital, Servicio Nacional de Geología y Minería, Publicación Geológica Digital, Santiago.

Camus, Francisco, Sillitoe, Richard M., Petersen, Richard (Eds.), 1998. Andean Copper Deposits: New Discoveries, Mineralization, Styles and Metallogeny. Society of Economic Geologists, pp. 119–129. https://doi.org/10.5382/SP.05.09.

Shirey, S.B., Walker, R.J., 1995. Carius tube digestion for low-blank rhenium-osmium analysis. Anal. Chem. 67, 2136–2141.

Sillitoe, R.H., 2010. Porphyry Copper Systems. Econ. Geol. 105, 3–41.

Skewes, A., Arévalo, A., Floody, R., Zúñiga, P., Stern, C., 2002. The giant El Teniente, breccia deposit: hypogene copper distribution and emplacement. In: In: Goldfarb, R.J., Nielsen, R.L. (Eds.), Integrated Methods for Discovery: Global Exploration in the 21st 9. Century. Society of Economic Geologists Special Publication, pp. 299–332.

Skewes, M.A., Stern, C.R., 1995. Genesis of the giant late Miocene to Pliocene copper deposits of central Chile in the context of Andean magmatic and tectonic evolution. Int. Geol. Rev. 37, 893–909.

Sláma, J., Košlera, J., Condon, D., Crowley, J., Gerdes, A., Hanchar, J., Horstwood, M., Morris, G., Nasdala, L., Norberg, N., Schaltegger, U., Schoene, B., Tubrett, M., Whitehouse, M., 2008. Plešovice zircon - A new natural reference material for U-Pb and Hf isotopic microanalysis. Chem. Geol. 249, 1–35.

Smoliar, M.I., Walker, R.J., Morgan, J.W., 1996. Re-Os ages of group IIA, IIIA, IVA, and IVB iron meteorites. Science 271, 1099–1102.

Solari, L., Gómez-Tuena, A., P., B.J., Pérez-Arvizu, O., Tanner, M., 2010. U-Pb zircon geochronology with an integrated LA-ICP-MS microanalytical workstation: achievements in precision and accuracy. Geostandards and Geoanalytical Research 34, 5–18.

Solari, L., González-León, C., Valencia-Moreno, M., Rascón-Heimpel, M., 2018. The Proterozoic of NW Mexico revisited: U-Pb geochronology and Hf isotopes of Sonoran rocks and their tectonic implications. Int. J. Earth Sci. 107, 845–861.

Somoza, R., Ghidella, M.E., 2005. Convergencia en el margen occidental de América del Sur durante el Cenozoico: subducción de las placas de Nazca, Farallón y Aluk. Revista de la Asociación Geológica Argentina 60, 797–809.

Spikings, R., Dungan, M., Foeken, J., Carter, A., Page, L., Stuart, F., 2008. Tectonic response of the central Chilean margin (35–38 degrees S) to the collision and subduction of heterogeneous oceanic crust: a thermochronological study. J. Geol. Soc. 165, 941–953.

Stein, H.J., Markey, R.J., Morgan, J.W., Hannah, J.L., Scherstén, A., 2001. The remarkable Re–Os chronometer in molybdenite: how and why it works. Terra Nova 13, 479–486.

Stern, C.R., Skewes, A., Arévalo, A., 2011. Genesis of igneous rocks associated with El Teniente Cu-deposit. J. Petrol. 52, 1591–1617.

Sun, W., Zhang, H., Ling, M.-X., Ding, X., Chung, S.-L., Zhou, J., Yang, X.-Y., Fan, W., 2011. The genetic association of adakites and Cu–Au ore deposits. Int. Geol. Rev. 53, 691–703.

Tassara, A., Echaurren, A., 2012. Anatomy of the Andean subduction zone: three-dimensional density model upgraded and compared against global-scale models. Geophys. J. Int. 189, 161–168.

Tassara, A., Götze, H.J., Schmidt, S., Hackney, R., 2006. Three-dimensional density model of the Nazca plate and the Andean continental margin. J. Geophys. Res. Solid Earth 111, B09404.

Vale-Exploraciones, 2017. Proyecto Arcángel. Reporte Temporada 2016-2017: Unpublished report., Santiago, p. 62.

Vergara, M., Morata, D., Hickey-Vargas, R., Lopez-Escobar, L., Beccar, I., 1999. Cenozoic tholeiitic volcanism in the Colbún area, Linares Precordillera, central Chile (35°35'-36°S). Revista geológica de Chile 26, 23–41.

Vervoort, J.D., Blichert-Toft, J., 1999. Evolution of the depleted mantle: Hf isotope evidence from juvenile rocks through time. Geochimica et Cosmochimica Acta 63 (3–4), 533–556.

Wiedenbeck, M., Alle, P., Corfu, F., Griffin, W.L., Meier, M., Oberli, F., von Quadt, A., Roddick, J.C., Spiegel, W., 1995. 3 natural zircon standards for U-Th-Pb, Lu-Hf, trace-element and REE analyses. Geostand. Geoanal. Res. 19, 1–23.

Yang, Z., Hou, Z., White, N.C., Chang, Z., Li, Z., Song, Y., 2009. Geology of the post-collisional porphyry copper–molybdenum deposit at Qulong, Tibet. Ore Geol. Rev. 36, 133–159.